

Ev-3DOD: Pushing the Temporal Boundaries of 3D Object Detection with Event Cameras

Hoonhee Cho*, Jae-young Kang*, Youngho Kim, and Kuk-Jin Yoon
KAIST

{gnsngsngml, mickeykang, kmax2001, kjyoon}@kaist.ac.kr

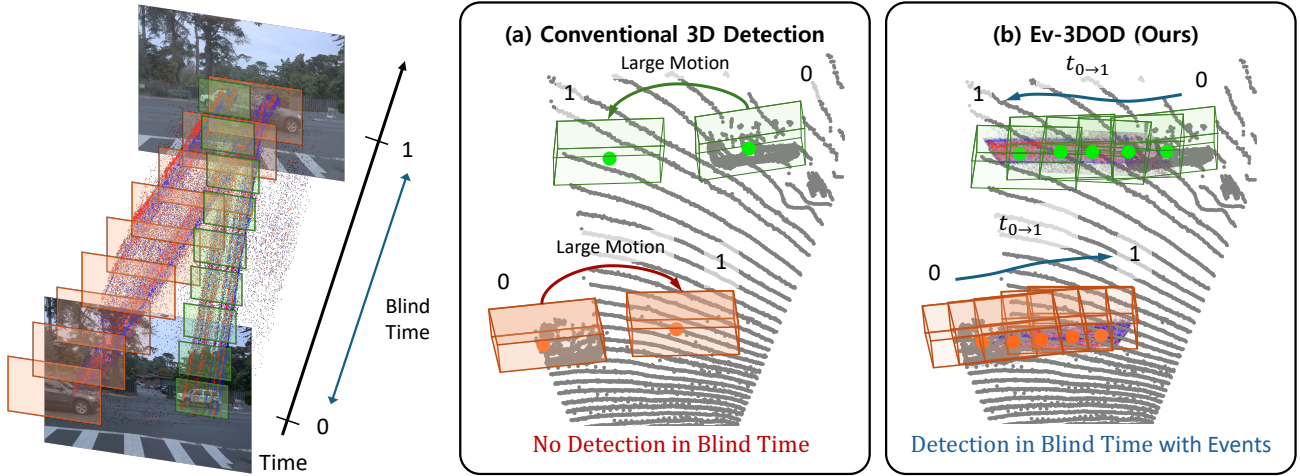


Figure 1. Comparison between the proposed Ev-3DOD and conventional 3D detection methods. Fixed frame rate sensors (e.g., LiDAR, frame camera) inevitably have periods of “blind time” ($t_{0 \rightarrow 1}$) when they lack data between active timestamps (0 and 1). Consequently, as shown in (a), conventional methods cannot detect objects during blind time, while other objects like vehicles can undergo significant motion within these gaps. In contrast, as illustrated in (b), our method, Ev-3DOD, leverages the high temporal resolution of the event camera, enabling accurate object detection even during the blind times of other sensors.

Abstract

Detecting 3D objects in point clouds plays a crucial role in autonomous driving systems. Recently, advanced multi-modal methods incorporating camera information have achieved notable performance. For a safe and effective autonomous driving system, algorithms that excel not only in accuracy but also in speed and low latency are essential. However, existing algorithms fail to meet these requirements due to the latency and bandwidth limitations of fixed frame rate sensors, e.g., LiDAR and camera. To address this limitation, we introduce asynchronous event cameras into 3D object detection for the first time. We leverage their high temporal resolution and low bandwidth to enable high-speed 3D object detection. Our method enables detection even during inter-frame intervals when synchronized data is unavailable, by retrieving previous 3D information through the event camera. Furthermore, we introduce the first event-based 3D object detection dataset, DSEC-3DOD, which includes ground-truth 3D bounding boxes

at 100 FPS, establishing the first benchmark for event-based 3D detectors. The code and dataset are available at <https://github.com/mickeykang16/Ev3DOD>.

1. Introduction

3D object detection is a crucial task in autonomous driving. Multi-modal sensors like LiDAR and cameras are commonly used to understand scenes and handle complex road scenarios. This sensor setup consists of synchronized sensors with a fixed frame rate and has limited speed due to bandwidth limitations. As shown in Fig. 1 (a), the blind time, which is the period when sensor information is unavailable (e.g., 100 milliseconds), is critical as cars can experience large motions as 3 meters during this time. Therefore, temporal resolution is a crucial factor that can directly influence accident risk.

Recently, event cameras [15] have introduced a new

*The first two authors contributed equally.

paradigm in perceptual research. Event cameras provide brightness changes as a stream of data in sub-millisecond latency, which makes them robust to motion blur [107] and have low bandwidth [19, 94]. Event cameras overcome the trade-off between bandwidth and blind time but have the drawback of sacrificing intensity information. To address this, recent work has combined event cameras with frame cameras to complement the sparsity of event cameras while overcoming the fixed frame rate sensor’s limits.

In this paper, we aim for accurate 3D object detection in blind time through a multi-modal approach that combines LiDAR and frame-based sensors with an event camera, leveraging its high temporal resolution. As shown in Fig. 1 (b), event data is available during blind times, while the LiDAR and image data from the most recent active timestamp are accessible. Therefore, there is a misalignment in timestamps between the fixed frame sensor data and the current blind time. Then, this raises the question: *how can we estimate 3D motion using only event data, especially in cases where data from other sensors aligned with the current time is unavailable?*

To address this, we propose a virtual 3D event fusion (V3D-EF) that transfers past 3D information to align with the present time using the event camera. As extensively covered in previous research [21, 38, 88], event data inherently contain motion information on an image plane. Based on this observation, we hypothesized that providing a 3D cue associated with the initial timestamp to the event information would enable accurate estimation of the 3D motion vector. To this end, we project event features into a 3D voxel space to create virtual 3D event features. In this process, events are projected only onto regions where point cloud data exists, aligning with the point cloud data. Then, we aggregate the event features with the voxel features to estimate an implicit motion field that captures the motion inherent within the grid. The generated implicit motion field encapsulates both the 3D spatial information from voxels and the motion information from events, enabling the calculation of a 3D motion vector from the most recent active timestamp to the present blind time.

Another crucial factor in 3D object detection is the score for each bounding box. The model considers both box proposal scores at the active timestamp and the motion score of each predicted box in blind time. In blind time, the model aligns 3D information of voxel features and motion information of events to learn the confidence of box motion.

A major hurdle in 3D detection research using event cameras is the lack of suitable datasets. To address this, we present two datasets: Ev-Waymo, which includes synthetic event data, and DSEC-3DOD, which contains real event data. Unlike existing public 3D object detection datasets, ours includes annotations not only for active timestamps with 3D LiDAR sensor data but also for blind times, pro-

viding annotation in 100 FPS frame rate.

2. Related Works

Single-modality 3D Object Detection. Given that cameras offer significant cost advantages over LiDAR sensors, many researchers have focused on developing methods that leverage camera-based systems for 3D object detection using image-only inputs [7, 10, 24, 28, 31, 36, 44, 52, 58–60, 63, 70, 92, 98, 100, 118]. Image-based 3D object detection faces challenges due to the lack of direct depth information. To overcome this challenge, several studies [7, 69, 75, 82, 99, 118] have employed depth estimation techniques to generate pseudo 3D point clouds or elevate 2D features into 3D space for object detection, alongside proposals for transformer-based architectures [33, 100, 123] that utilize 3D object queries and 3D-2D correspondences. Nonetheless, accurately estimating depth from images remains difficult, resulting in image-based methods performing worse than LiDAR-based approaches.

LiDAR-based 3D object detection can reliably estimate 3D bounding boxes using point clouds captured from LiDAR sensors. Current LiDAR-based detection methods can be divided into three categories based on different point cloud encoding formats: point-based methods [14, 30, 78, 79, 81, 85, 87, 109, 114, 126], voxel-based methods [4, 12, 13, 23, 27, 27, 29, 41, 47, 53, 64, 65, 84, 101, 104, 113, 120, 128], and point-voxel fusion networks [6, 26, 67, 86, 108]. While LiDAR detection is advantageous in various conditions, it often struggles in areas with sparse LiDAR data. Therefore, integrating the geometric benefits of point clouds with the semantic richness of images remains crucial for improving performance.

Multi-modality 3D Object Detection. Multi-modal sensor fusion [5, 32, 34, 45, 46, 54, 55, 57, 91, 102, 103, 116], where different sensors complement each other, typically utilizes a combination of cameras and LiDAR. Multimodal 3D object detection has gained attention for improving accuracy over unimodal methods. Fusion approaches are categorized into early [3, 11, 40, 80, 95, 105], middle [49–51, 56, 62, 76, 77, 110, 124], and late fusions [1, 45, 68], with middle fusion now preferred due to its robustness to calibration errors and enhanced feature interaction. Cross-modal fusion has achieved significant performance improvements by enhancing the sparse features of point clouds with semantic information from images. However, there are still unexplored areas concerning safety in autonomous driving. LiDAR and cameras have limited time resolution (*i.e.*, 10-20 Hz) due to the relatively high bandwidths. To enhance safety, algorithms that operate at high speeds are essential. To address this, we introduce an asynchronous event camera with high temporal resolution for 3D object detection for the first time. The proposed method performs multi-modal fusion between synchronized sensors

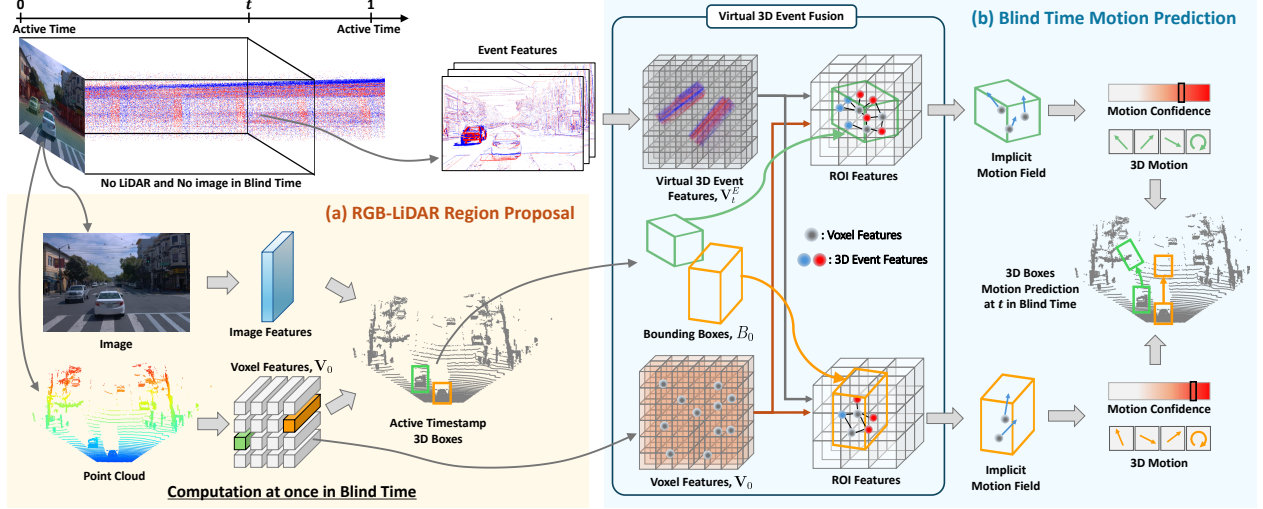


Figure 2. The overall pipeline for event-based 3D object detection (Ev-3DOD). (a): At active timestamp 0, LiDAR and image data are available. Therefore, we utilize an RGB-LiDAR Region Proposal Network (RPN) to extract voxel features and 3D bounding boxes at the active timestamp. (b): To predict the bounding box during blind time, $0 \leq t < 1$, we estimate the 3D motion and confidence score using event features. For computational efficiency, we design the process to compute (a) only once before the next active timestamp while performing iterative computations solely for (b).

and asynchronous events to increase the operational frequency of 3D detection.

Event-based Object Detection. Event cameras break through the limitations of bandwidth requirements and perceptual latency with the trade-off of sparse data and loss of intensity information. To make the most of these characteristics, prior work has designed models to adapt to event data using graph neural networks [2, 16, 17, 48, 83], spiking neural networks [111, 122], and sparse neural networks [66, 73]. Recently, effective dense neural networks [25, 35, 43, 71, 74, 97, 130] and transformer architectures [19, 42, 72, 73] have been developed to leverage event cameras, aiming to achieve both low latency and high performance. These advances enable real-time operation with impressive accuracy, demonstrating the practical applicability of event cameras in real-world scenarios. To the best of our knowledge, we are the first to extend event-based object detection from 2D to 3D space. By employing a multi-modal fusion approach of the event camera and 3D sensors (*i.e.*, LiDAR), we aim to overcome the latency and persistent interval time barriers of 3D object detections.

3. Method

3.1. Problem Definition.

LiDAR and camera data are only available at active timestamps 0 and 1, where 1 represents invalid future information in an online process. Our goal is to predict 3D bounding boxes during $0 \leq t < 1$, including the blind time when synchronized sensors are unavailable. Given a pair of synchronized 3D points $P_0 = \{(x_l, y_l, z_l)\}_{l=1}^N$ and image

$I_0 \in \mathbb{R}^{3 \times H \times W}$ at active timestamp 0, we leverage event stream $\mathcal{E}_{0 \rightarrow t} = \{(i, j, p, \tau) | 0 \leq \tau < t\}$ to detect 3D bounding box set B_t at an arbitrary time $0 \leq t < 1$.

3.2. Framework Overview

As illustrated in (a) of Fig. 2, at active timestamp 0, both LiDAR and image data are available. RGB-LiDAR Region Proposal Network (RPN) generates bounding box proposals from rich 3D information in active time. We begin by voxelizing the point cloud and generating voxel features, denoted as $\mathbf{V}_0 \in \mathbb{R}^{D_X \times D_Y \times D_Z \times C}$, where D_X , D_Y , and D_Z represent the grid size, and C denotes the channel dimension, using a 3D backbone [128]. Then, using existing region proposals [117] and refinement networks [45] with image features, we generate bounding box proposals, $B_0 = \{B_0^1, B_0^2, \dots, B_0^n\}$ and box proposal confidence $p_0 = \{p_0^1, p_0^2, \dots, p_0^n\} \in [0, 1]$ for the active timestamp 0. RGB-LiDAR-based multi-modal networks have been widely studied, leading to many advanced models capable of accurate estimation at active timestamps. We tuned the model with fewer parameters and a reduced channel dimension to improve efficiency.

Our emphasis is on achieving precise estimation throughout the blind time, spanning the interval from active timestamp 0 to the subsequent timestamp 1. To infer bounding boxes at an arbitrary inter-frame time t , we first convert the event stream, $\mathcal{E}_{0 \rightarrow t}$ into voxel grids [129] as \mathbb{E}_t . Then, we use a feature encoder to produce event features, $\mathbf{E}_t \in \mathbb{R}^{H/4 \times W/4 \times C}$, where H and W is the spatial dimensions of the events. Our objective is to estimate the 3D motion of objects during blind time. To achieve

this, we utilize the bounding box set B_0 and voxel features \mathbf{V}_0 from the active timestamp 0. During blind times, we share the voxel features, \mathbf{V}_0 , generated at the active timestamp, ensuring that voxel features are computed only once to maintain a cost-effective structure. Through the Virtual 3D Event Fusion (V3D-EF), we generate an implicit motion field for each bounding box by integrating event and voxel features, encapsulating motion information. Using this field, we compute the 3D motion and confidence score, enabling the estimation of 3D boxes at the blind time t .

3.3. Virtual 3D Event Fusion for Motion Prediction

The event feature continuously captures each pixel’s motion information over time on the 2D image plane. However, estimating 3D motion using only events is a challenge. We hypothesize that providing each event feature with adequate 3D information would allow for effective 3D motion estimation. To achieve this, we aim to incorporate a 3D cue into the event features. Since both event features and voxel features are sparse, it is crucial to align each voxels with the corresponding events accurately. Directly using the voxel features would cause misalignment with the actual 3D geometry. Thus, we adopt the voxel point centroid method employed in previous works [30].

Specifically, we first consider the non-empty voxel features as $\mathbf{V}_0 = \{V_0^k = \{h_0^k, f_0^k\} \mid k = 1, \dots, N_V\}$, where h_0^k is the 3D voxel index, f_0^k is the associated voxel feature vector, and N_V is the number of non-empty voxels. Then, points within each voxel are grouped into a set $\mathcal{N}(V_0^k)$ by determining their voxel index h_0^k based on their spatial coordinates $X_i = (x_i, y_i, z_i)$ of points. The centroid of each voxel feature is subsequently computed as:

$$c_0^k = \frac{1}{|\mathcal{N}(V_0^k)|} \sum_{X_i \in \mathcal{N}(V_0^k)} X_i. \quad (1)$$

The centroid c_0^k is calculated for non-empty voxels, ensuring it corresponds only to indices with existing points, with the goal of aligning these centroids to the event data. As shown in the top of Fig. 3, we propose a method to project events into a virtual voxel space based on the coordinates of the centroids. The projection onto the image plane from 3D space can be obtained as: $\mathbf{p}_0^k = K \cdot E \cdot c_0^k$, where K and E denote the intrinsic and extrinsic parameters, \cdot operation is matrix multiplication. Therefore, we calculate the event coordinates corresponding to each centroid, c_0^k , and gather the event features, \mathbf{E}_t , at these coordinates, \mathbf{p}_0^k , to create virtual 3D event features, $\mathbf{V}_t^E = \{\mathbf{E}_t(\mathbf{p}_0^k)\}_{k=1}^{N_V} \in \mathbb{R}^{N_V \times C}$.

Since we aim to estimate the 3D motion of bounding boxes from the active timestamp 0 up to the current time t , we consider fusion only for the features corresponding to the box proposal. Given the bounding box proposals, B_0 , at active timestamp 0, we divide box proposals into

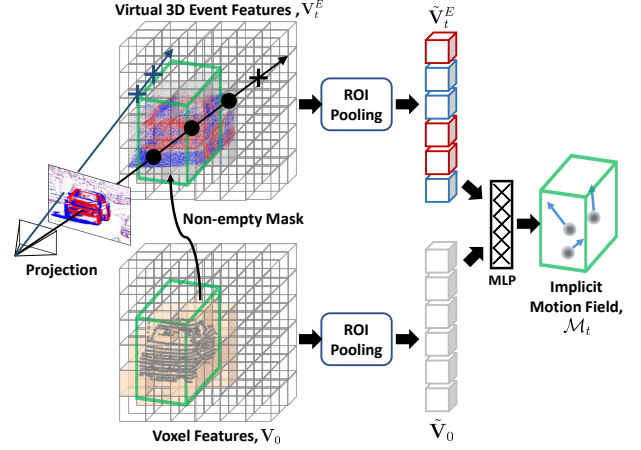


Figure 3. Virtual 3D Event Fusion (V3D-EF). We generate an implicit motion field for each bounding box by applying the ROI pooling separately to the virtual 3D event features, which represent the 3D projection of events, and the voxel features.

$S \times S \times S$ regular sub-voxels. Then, we independently perform the ROI pooling [12] on the virtual 3D event features \mathbf{V}_t^E , and the voxel features \mathbf{V}_0 , corresponding to each sub-voxel. This generates grid features for the bounding boxes, denoted as $\tilde{\mathbf{V}}_t^E \in \mathbb{R}^{n \times S^3 \times C}$ and $\tilde{\mathbf{V}}_0 \in \mathbb{R}^{n \times S^3 \times C}$, where n is the number of box proposals. The generated features are then concatenated and passed through an MLP to produce the implicit motion field, $\mathcal{M}_t = \{\mathcal{M}_t^0, \mathcal{M}_t^1, \dots, \mathcal{M}_t^n\}$. The implicit motion field is created by aligning 3D events with their corresponding voxel features, encapsulating motion information for the bounding box. Using an MLP, we estimate the explicit 3D motion. The explicit box motion $\mathbf{M}_{0 \rightarrow t}^i = (dx^i, dy^i, dz^i, d\alpha^i)$, defined in box local coordinate of B_0^i , contains spatial shift and yaw rotation. The final box location is calculated as $B_t^i = g(B_0^i, \mathbf{M}_{0 \rightarrow t}^i)$, where g is a box shifting operation.

3.4. Motion Confidence Estimator

As discussed in previous studies [117, 128], self-awareness of the confidence of predicted bounding boxes is a key factor. The simplest choice of final confidence score in our setting would be the score of active timestamp 0. However, the final score should take into account the object’s motion prediction during the blind time. If the object experiences challenging motion during the blind time, a reliable bounding box at the active timestamp 0 could become less reliable. Therefore, the final score should consider two different sources. The first aspect is the score estimated at the active timestamp, based on LiDAR and images. The second aspect is the confidence score based on motion during the blind time using events.

The implicit motion field from Sec. 3.3 contains 3D motion information through alignment between the point

cloud and events. We additionally employ an MLP specifically for calculating motion confidence. Box-wise motion confidence is estimated and normalized, resulting in $p_{0 \rightarrow t} = \{p_{0 \rightarrow t}^1, p_{0 \rightarrow t}^2, \dots, p_{0 \rightarrow t}^n\} \in [0, 1]$. The final confidence score for box proposal i is calculated by considering both the score at the active timestamp and the motion confidence:

$$p_t^i = p_0^i \cdot p_{0 \rightarrow t}^i. \quad (2)$$

3.5. Training Objectives

For RGB-LiDAR RPN in the active timestamp, we follow RPN loss from [45, 106, 117]. For blind time prediction, box regression loss from [117] is applied between the predicted 3D box B_t^i and the ground-truth \hat{B}_t^i . The target assigned to the motion confidence branch is an IoU-related value, as:

$$\hat{p}_{0 \rightarrow t}^i(\text{IoU}_i) = \begin{cases} 0 & \text{if } \text{IoU}_i < \theta_L, \\ \frac{\text{IoU}_i - \theta_L}{\theta_H - \theta_L} & \text{if } \theta_L \leq \text{IoU}_i < \theta_H, \\ 1 & \text{if } \text{IoU}_i \geq \theta_H, \end{cases}$$

IoU_i is the IoU between the i -th prediction and the corresponding ground truth box, while θ_H and θ_L are foreground and background IoU thresholds. Binary Cross Entropy Loss is exploited here for confidence prediction. The losses of our detect head are computed as:

$$\mathcal{L} = \mathcal{L}_{RPN} + \lambda_1 \cdot \mathcal{L}_{reg} + \lambda_2 \cdot \mathcal{L}_{score} \quad (3)$$

4. Event-based 3D Object Detection Datasets

This study is the first to explore the utilize event camera for 3D detection. To validate our model’s effectiveness, we introduce two event 3D detection datasets: Ev-Waymo, which consists of synthetic events, and DSEC-3DOD with real events. We first obtained accurate 3D bounding box annotations for the active time, when both LiDAR and image data are available, and then processed the blind time.

4.1. Annotation for Active Time at 10 FPS

Ev-Waymo Dataset is a synthetic event dataset based on the Waymo Open Dataset (WOD) [93]. WOD provides sequential pairs of synchronized LiDAR, image data, and 3D box annotations at 10 FPS. Event streams are generated using a widely-adopted event simulator [18]. The Ev-Waymo evaluation follows the same metrics as WOD, calculating both average precision (AP) and average precision weighted by heading (APH). Adhering to the DSEC-3DOD setting, Ev-Waymo employs the front camera and a cropped LiDAR aligned to the corresponding field of view.

DSEC-3DOD. The DSEC dataset [20] is a stereo event dataset that includes LiDAR, image, and real event data captured in challenging environments. We sampled a portion

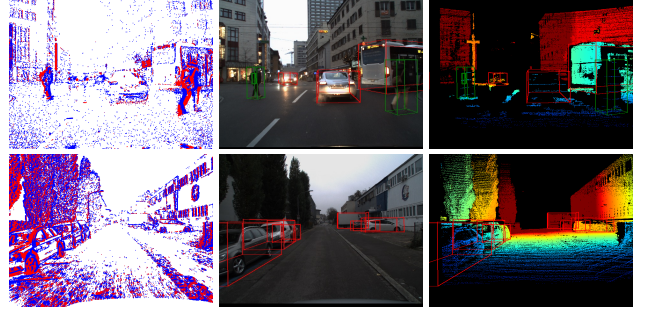


Figure 4. DSEC 3D Object Detection Dataset samples. Event data, label overlaid image, and accumulated LiDAR from left to right.

of the “zurich_city” sequence, providing LiDAR and image data at 10 FPS. We hired annotation experts to label 3D bounding boxes at 10 FPS, ensuring alignment with the sensor data. As shown in Fig. 4, in the annotation process, we used accumulated LiDAR points to enable the precise generation of ground-truth 3D bounding boxes. For evaluation on DSEC-3DOD, we used the same evaluation metrics as Ev-Waymo but include only vehicle and pedestrian classes due to a lack of cyclist data, with all objects categorized under a single difficulty level.

4.2. Annotation for Blind Time at 100 FPS

For training and evaluation on 3D detection during blind time, we created 3D box annotations for periods when LiDAR and images were absent. We linearly interpolated the original 10 FPS annotations, dividing blind times into 10 evenly spaced intervals between consecutive frames, resulting in temporally dense annotations at 100 FPS. To ensure accurate bounding box ground-truths in instances where LiDAR and image data are unavailable, we employed event-based video frame interpolation [37] and point cloud interpolation [125] methods to generate sensor data for blind time. Data annotation experts refined interpolated bounding boxes based on the generated sensor data. The Ev-Waymo dataset consists of 80 sequences comprising a total of 157K labeled scenes, providing 100 FPS detection ground-truth. The DSEC 3D dataset consists of 178 sequences and includes 54K labeled scenes. For evaluation in blind time, we utilize all ground truth boxes at 100 FPS. More details of the datasets are described in the supplementary material.

5. Experiments

5.1. Experiment Setup

We target causal 3D detections to detect objects during blind time. For comparison, we present two types of evaluation methods for conventional models. First is the online evaluation, where the network is inferred at any given blind time using only accessible data. Conventional methods can

Table 1. Performance comparison on the Ev-Waymo dataset for 3D vehicle (IoU = 0.7), pedestrian (IoU = 0.5) and cyclist (IoU = 0.5) detection following previous protocols. Evaluated on 100 FPS ground-truth annotation for $t = \{0, 0.1, \dots, 0.9\}$. Offline represents results obtained by interpolating data using sensor data from active timestamps 0 and 1. Online represents results obtained using data accessible at present. Specifically, online evaluation of previous works uses only the data from active timestamp 0, while we also utilize event data from active timestamp 0 up to the present time.

	Interpolation Methods	Methods	3D Detection Modality	ALL (mAP/mAPH)	VEH (AP/APH)		PED (AP/APH)		CYC (AP/APH)	
				L2	L1	L2	L1	L2	L1	L2
Offline	N-PCI [125]	VoxelNeXt [9]	L	53.61/50.67	62.96/62.51	59.10/58.67	68.43/60.77	62.85/55.69	44.55/43.15	38.88/37.65
		HEDNet [121]	L	50.52/47.51	59.57/59.09	55.90/55.45	63.28/55.32	58.03/50.62	43.14/41.80	37.63/36.46
	N-PCI [125] + EMA [119]	Focals Conv [8]	L + I	42.53/40.41	55.49/55.02	54.45/53.99	48.07/43.06	46.54/41.69	27.70/26.60	26.59/25.54
		LoGoNet [45]	L + I	53.29/50.49	63.48/63.05	60.15/59.73	67.85/60.28	62.43/55.37	42.40/41.37	37.29/36.38
	N-PCI [125] + CBM [37]	Focals Conv [8]	L + I	42.51/40.39	55.48/55.01	54.44/53.98	48.07/43.06	46.54/41.68	27.67/26.57	26.56/25.50
		LoGoNet [45]	L + I	53.57/50.75	63.60/63.16	60.27/59.85	68.14/60.53	62.77/55.67	42.85/41.81	37.66/36.74
Online	N/A	VoxelNeXt [9]	L	33.32/31.70	44.40/44.10	41.78/41.49	40.52/36.23	36.93/32.96	24.40/23.73	21.24/20.66
		HEDNet [121]	L	31.57/29.90	42.03/41.71	39.32/39.02	38.86/34.43	35.67/31.53	22.64/21.99	19.72/19.14
		Focals Conv [8]	L + I	26.27/25.01	37.31/37.01	36.60/36.31	29.20/26.16	28.41/25.44	14.30/13.78	13.79/13.29
		LoGoNet [45]	L + I	33.27/31.75	44.14/43.87	41.73/41.47	39.98/35.84	36.48/32.67	24.71/24.15	21.59/21.10
		Ev-3DOD (Ours)	L + I + E	48.06/45.60	60.30/59.95	59.19/58.85	57.40/50.78	55.30/48.93	31.08/30.38	29.69/29.03

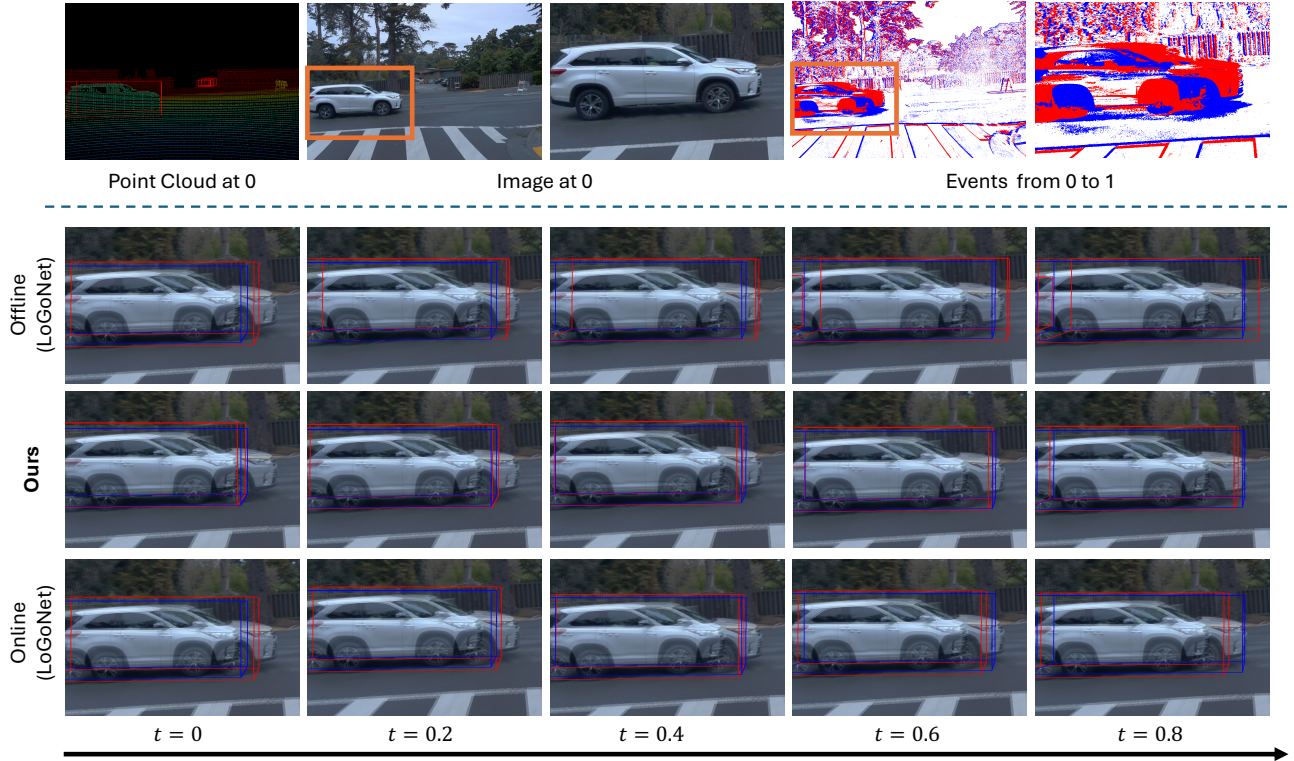


Figure 5. Qualitative comparisons of our method with other offline and online evaluations on the Ev-Waymo dataset. $t = 0$ represents the active time, while $t = 0.2, 0.4, 0.6, 0.8$ denotes the blind times. The blue box represents the ground truth, while the red box shows the prediction results of each method. For easier understanding, images at active timestamps 0 and 1 are overlaid.

only process the most recent sensor data at active timestamp 0. In contrast, our approach additionally incorporates event data from active timestamp 0 up to the current blind time. Second, offline evaluation addresses the challenge of applying conventional fixed-frame-rate approaches directly to blind time by utilizing future data. In other words, data for the blind time is interpolated using active timestamps 0 and

1, where timestamp 1 represents future data. Consequently, these offline evaluations serve as a performance oracle for online methods. More implementation details are provided in the supplementary material.

Table 2. Results on the DSEC-3DOD dataset for 3D vehicle (IoU = 0.7), and pedestrian (IoU = 0.5) detection.

	Interpolation Methods	Methods	3D Detection Modality	ALL		VEH		PED	
				mAP	mAPH	AP	APH	AP	APH
Offline	N-PCI [125]	VoxelNeXt [9]	L	36.29	32.43	45.35	44.93	27.23	19.93
		HEDNet [121]	L	37.73	30.73	41.82	41.35	33.64	20.1
	N-PCI [125] + EMA [119]	Focals Conv [8]	L + I	30.29	25.85	35.52	35.04	25.05	16.65
		LoGoNet [45]	L + I	37.30	31.39	44.64	44.06	29.96	18.72
	N-PCI [125] + CBM [37]	Focals Conv [8]	L + I	30.28	25.86	35.56	35.08	24.99	16.64
		LoGoNet [45]	L + I	37.35	31.45	44.76	44.17	29.94	18.73
Online	N/A	VoxelNeXt [9]	L	13.94	12.90	21.42	21.23	6.46	4.57
		HEDNet [121]	L	13.75	11.68	18.48	18.29	9.02	5.07
		Focals Conv [8]	L + I	10.81	9.61	15.74	15.55	5.88	3.67
		LoGoNet [45]	L + I	13.29	11.91	19.50	19.32	7.07	4.49
		Ev-3DOD (Ours)	L + I + E	31.17	26.54	41.65	41.20	20.68	11.88

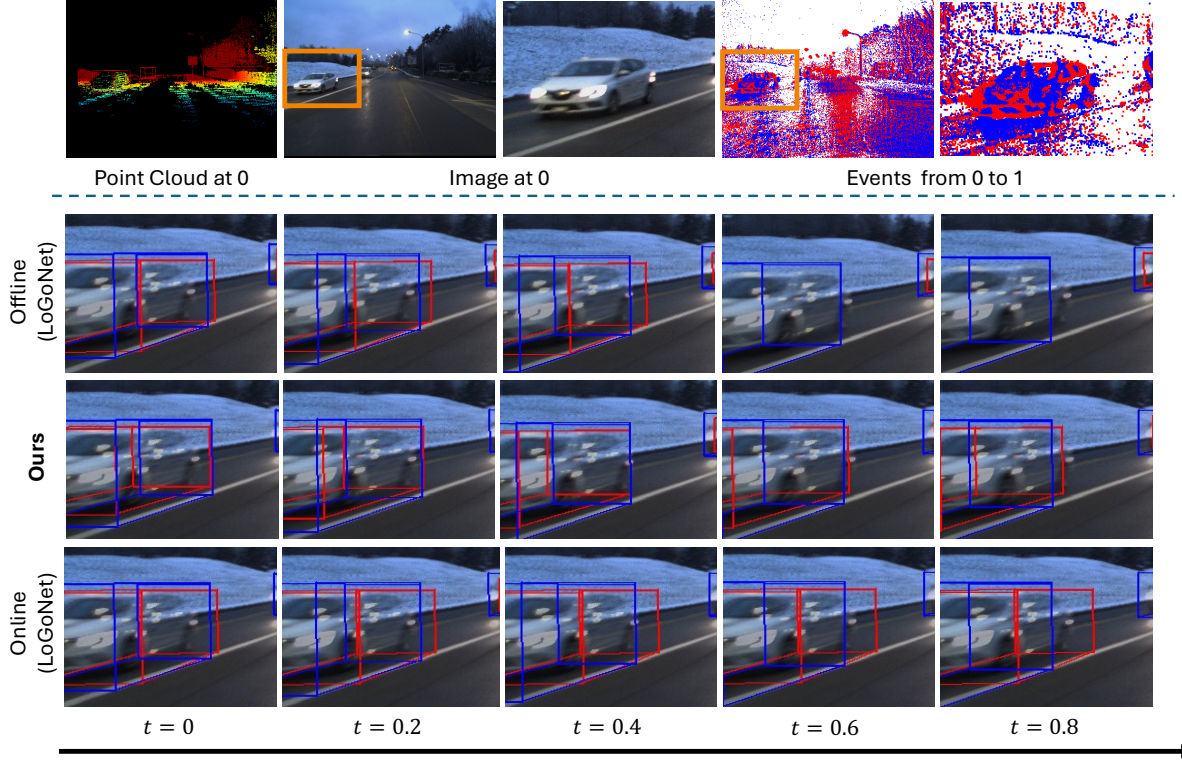


Figure 6. Qualitative comparisons of our method with other offline and online evaluations on the DSEC-3DOD dataset. $t = 0$ represents the active time, while $t = 0.2, 0.4, 0.6, 0.8$ denotes the blind times. The blue box represents the ground truth, while the red box shows the prediction results of each method. For easier understanding, images at active timestamps 0 and 1 are overlaid.

5.2. Experimental Results

We employ recent state-of-the-art approaches, including LiDAR-based [9, 121] and LiDAR-camera-based multi-modal methods [8, 45]. For the offline image interpolation, we utilize frame-based, EMA [119], and the event-based method, CBM [37]. NeuralPCI [125] is adopted for point cloud interpolation.

Ev-Waymo. Table 1 shows the quantitative result of Ev-Waymo. Comparing methods in the online setting, previous methods [8, 9, 45, 121], which rely on fixed-frame-rate sensors (*i.e.*, LiDAR and Image), cannot detect object motion during blind times. This limitation leads to reduced performance when evaluated with 100 FPS ground-truth. In

contrast, our approach, leverages high-temporal resolution of event data to estimate object motion during blind time, significantly outperforming existing online methods. Notably, Ev-3DOD is comparable to offline oracles and even surpasses the performance of a certain approach [8].

Figure 14 shows comparisons between the results of online, offline, and our method during blind time. Existing online methods fail to align prediction with the ground truth during blind time. In contrast, Ev-3DOD, despite being an online approach, aligns well with the ground-truth and demonstrates performance comparable to offline methods.

DSEC-3DOD. As shown in Table 2, we evaluate our model on the DSEC-3DOD real event dataset, which includes fast motion and challenging lighting conditions that sig-

Table 3. Ablation study of the proposed components.

V3D-EF	MCE	L2	
		mAP	mAPH
		33.30	31.68
✓		<u>46.55</u>	<u>44.22</u>
✓	✓	48.06	45.60

Table 4. Effectiveness of non-empty mask in the V3D-EF module.

Method	L2	
	mAP	mAPH
w/o Non-empty Mask	42.57	40.50
w/ Non-empty Mask	46.55	44.22

nificantly degrade performance during blind time. Our model effectively estimates the 3D motion of objects from events, achieving a substantial improvement over other on-line methods. Notably, it demonstrates performance comparable to offline oracle methods that utilize future information. The analysis of computational complexity is provided in the supplementary material.

Figure 6 shows blind time detection inference for fast-moving objects in the DSEC dataset. Under low-light conditions and rapid motion, the quality of the interpolated pseudo-sensor data may deteriorate, occasionally resulting in detection failures, even when future information is utilized. In contrast, the proposed Ev-3DOD accurately detects objects in blind time, predicting motion from events.

5.3. Ablation Study and Analysis

We present an ablation study on key components and various analyses on the Ev-Waymo dataset. In V3D-EF analyses, the motion confidence estimator (MCE) module is excluded for clear comparisons.

Effectiveness of Each Component. In Table 3, we conduct the ablation study on the key components of Ev-3DOD. We evaluated a baseline and progressively added modules to observe improvements. The motion confidence estimator is dependent on V3D-EF, so it was not evaluated separately. V3D-EF, which explicitly estimates motion, has a direct impact on performance, resulting in significant improvements of +13.25% in mAP and +12.54% in mAPH. Additionally, the motion confidence estimator refines prediction scores at each blind time, demonstrating its effectiveness with further gains of +1.51% and +1.38%, respectively.

Non-empty Mask in V3D-EF. In the proposed V3D-EF, we employ a non-empty mask to achieve accurate and efficient alignment between sparse events and voxel features. To demonstrate the effectiveness of this non-empty mask, we conduct a comparative experiment in which events are projected onto all voxels within the V3D-EF module. The results in Table 4 confirm that the non-empty mask enables effective alignment between the two modalities.

Variations of the V3D-EF module. Our core component, the V3D-EF module, offers several design choices. To ana-

Table 5. Comparison of results across different modalities and fusion variants of the V3D-EF module.

Method	L2	
	mAP	mAPH
Base Model	33.30	31.68
+ LiDAR	37.04	35.25
+ Event	42.23	40.17
+ LiDAR + Event (fusion before pooling)	<u>43.95</u>	<u>41.87</u>
+ LiDAR + Event (fusion after pooling)	46.55	44.22

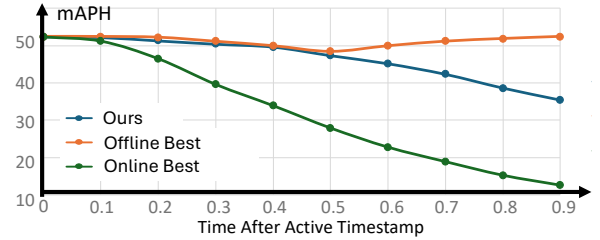


Figure 7. Detection performance over time elapsed since the active timestamp. We compare ours with offline and online approaches.

lyze these, we designed various variants, presenting the results accordingly. Our core component, the V3D-EF module, provides multiple design options. To analyze these configurations, we developed and evaluated several variants, with the results summarized in Table 5. We experimented with generating the implicit motion field using each modality, *i.e.*, LiDAR and event sensors, and found a performance drop compared to the multi-modal approach. This decline is likely due to the limitations of each modality: LiDAR alone cannot capture motion information during blind times, and event features cannot accurately estimate refined 3D motion. Additionally, multi-modal fusion before pooling decreased performance. We believe this is because fusing before pooling leads to integration between voxels and events outside of box proposal regions, resulting in the use of redundant and possibly misaligned information.

Detection Performance per Elapsed Blind Time. Figure 7 shows the detection performance over time elapsed since the active timestamp. Due to object motion, the performance of online detection deteriorates rapidly as the time distance from the active timestamp increases. In contrast, offline methods sustain robust performance throughout the blind time by leveraging future data, with only a slight performance drop at the center of the blind time as it moves further from the active timestamps located at both ends. The proposed model, relying solely on event data, achieves a temporal degradation pattern comparable to that of the offline method.

6. Conclusions

This paper proposes Ev-3DOD, a novel method to utilize an event camera in 3D detection for detecting objects in blind time. To transfer information from active times to the cur-

rent blind time, we estimate 3D motion based on event data. To effectively fuse sparse LiDAR data with events, we propose a Virtual 3D Event Fusion (V3D-EF) and introduce a motion confidence estimator to define confidence for 3D detection during blind times. For this study, we introduce the first event-based 3D detection dataset, emphasizing its 100 FPS annotations. We hope this work showcases the potential of neuromorphic cameras, inspiring future research.

Ev-3DOD: Pushing the Temporal Boundaries of 3D Object Detection with Event Cameras

Supplementary Material

In this supplementary material, we offer more details of our work, Ev-3DOD. Specifically, we provide

- Implementation details in Section 7;
- Runtime analysis of our framework, Ev-3DOD, in Section 8;
- Detailed processing and annotation processes about event-based 3D detection datasets in Section 9;
- Additional qualitative results and video demo in Section 10;
- Hyper-parameter analysis in Section 11;

7. Implementation Details

The model is trained using a two-stage strategy inspired by previous works [45, 115] that leverages pre-trained encoders. In the first stage, 10 FPS LiDAR and images are utilized to train the active timestamp RGB-LiDAR Region Proposal Network. In the second stage, all sensor data are incorporated to train the blind time modules with 100 FPS ground truth bounding boxes. In the first stage, the Region Proposal Network is trained for 15 epochs with a batch size of 4 and a learning rate of 0.001, using the Adam optimizer [39] with the scheduling strategy from [90]. In the second stage, the blind time modules are trained for 15 epochs with a batch size of 3, maintaining the same learning rate of 0.001. The loss function incorporates weights $\lambda_1 = 1.0$ and $\lambda_2 = 1.0$.

Since only the front camera is used, we followed the KITTI [22] methodology, utilizing only LiDAR point clouds and ground truth that fall within the camera’s field of view. The point cloud spans $[0.0, 75.2m]$ along the X axis, $[-75.2m, 75.2m]$ along the Y axis, and $[-2m, 4m]$ along the Z axis, with a voxel size of $(0.1m, 0.1m, 0.15m)$. Ev-Waymo uses a resolution of 960×640 , while DSEC-3DOD

adopts 320×240 for both images and events using a down-sample. The event stream is converted into a voxel grid with 5 bins.

Waymo provides dense LiDAR data with 64 channels, whereas DSEC has only 16 channels, making it significantly sparser. Due to this sparsity, we attempted to accumulate LiDAR frames, but previous methods still struggled to train stably. Consequently, following prior works [96, 127], we used disparity maps to generate 3D points instead of directly utilizing raw LiDAR data. We acknowledge that these disparity-based 3D points are obtained through offline processing. However, the key focus of this work is not to achieve state-of-the-art performance using LiDAR but to demonstrate the feasibility of blind time object detection using event cameras. Therefore, using these 3D points does not pose an issue for our study. Nevertheless, to enhance the usability of DSEC-3DOD dataset for future research, we have conducted additional experiments using raw LiDAR data and have shared the results at the following link¹.

The voxel data is encoded using a 3D backbone [128], while the image and event data are processed using a common image encoder [61]. The small version of our model is discussed in Section 8. In the Virtual 3D Event Fusion module, each box proposal is divided into $6 \times 6 \times 6$ sub-voxels.

8. Inference Time

To measure the inference time of our method and other approaches, we followed the speed measurement protocol from conventional event-based object detection [19], using the code provided at the given link². We also performed

¹<https://github.com/mickeykang16/Ev3DOD/tree/main/Benchmark>

²<https://github.com/uzh-rpg/RVT>

Table 6. Performance and runtime comparison on the Ev-Waymo dataset. Evaluated at 100 FPS for $t = 0, 0.1, \dots, 0.9$. Offline results, which rely on sensor data from timestamp 1, future information, and additional interpolation algorithms, are excluded from evaluation.

Methods	3D Detection Modality	ALL (mAP/mAPH)	VEH (AP/APH)		PED (AP/APH)		CYC (AP/APH)		FPS
		L2	L1	L2	L1	L2	L1	L2	
VoxelNeXt [9]	L	33.32/31.70	44.40/44.10	41.78/41.49	40.52/36.23	36.93/32.96	24.40/23.73	21.24/20.66	17.34
HEDNet [121]	L	31.57/29.90	42.03/41.71	39.32/39.02	38.86/34.43	35.67/31.53	22.64/21.99	19.72/19.14	12.84
Focals Conv [8]	L + I	26.27/25.01	37.31/37.01	36.60/36.31	29.20/26.16	28.41/25.44	14.30/13.78	13.79/13.29	6.08
LoGoNet [45]	L + I	33.27/31.75	44.14/43.87	41.73/41.47	39.98/35.84	36.48/32.67	24.71/24.15	21.59/21.10	10.68
Ev-3DOD (Ours)	L + I + E	48.06/45.60	60.30/59.95	59.19/58.85	57.40/50.78	55.30/48.93	31.08/30.38	29.69/29.03	27.09
Ev-3DOD- <i>Small</i> (Ours)	L + I + E	44.21/42.01	57.95/57.62	56.89/56.57	51.87/45.91	49.94/44.21	27.01/26.44	25.80/25.25	54.14

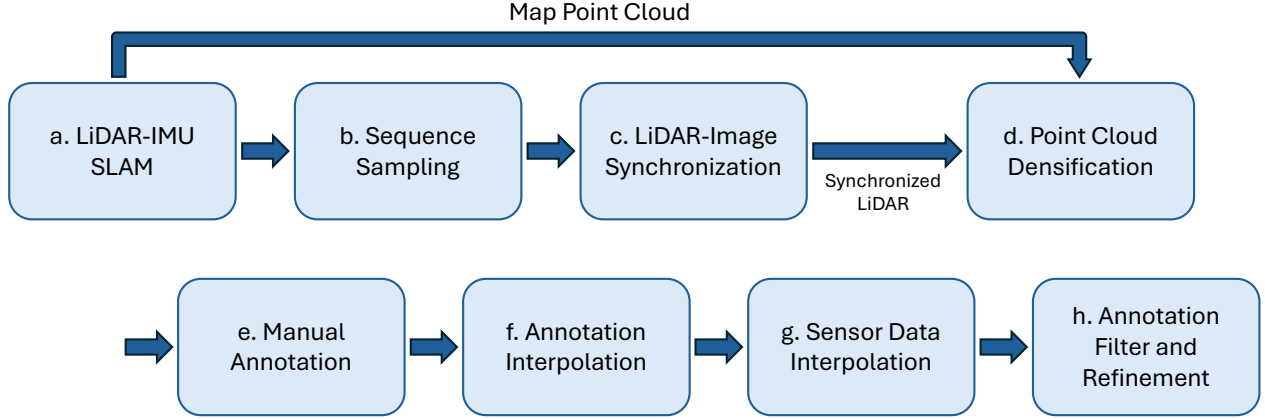


Figure 8. The overall pipeline for annotation. To enhance data quality, we perform software-based alignment and generate fine-grained 100 FPS ground-truths through additional annotation and post-processing.

GPU warm-up and ensured GPU-CPU synchronization using ‘torch.cuda.synchronize()’ to accurately measure inference time. We measured inference time on a single NVIDIA A6000 GPU with a batch size of 1 and additionally designed a lightweight model, *Ev-3DOD-Small*, to evaluate both performance and speed. Specifically, *Ev-3DOD-Small* retains the overall structure of *Ev-3DOD* but replaces the event feature encoder with three simple convolution layers, reduces the number of pooling layers, and decreases the grid size in the Virtual 3D Event Fusion module.

Table 6 compares performance and inference time among online methods. Looking at the performance metrics, our method, leveraging the event camera to infer during the blind time, achieves the best and second-best results across both approaches, with a significant margin over other methods. In terms of inference time, measured in FPS, even our full model (*Ev-3DOD*) achieves the fastest speed compared to other methods. This efficiency is attributed to our approach, which avoids recalculating point clouds and images during the blind time interval by explicitly leveraging events to update and reuse data at the present moment, making it highly cost-effective. Notably, when parameters are reduced, there is almost a twofold improvement in FPS with minimal performance degradation. This demonstrates that our method can effectively estimate 3D motion using event information without relying on a large number of parameters. We believe that the proposed *Ev-3DOD*, with its fast runtime using the high-frequency properties of an event camera, provides a promising direction for advancing future research in 3D object detection using event cameras.

9. Event-based 3D Object Detection Datasets

In this section, we provide additional details about the dataset that may not have been fully covered in the main pa-

per. Specifically, we delve into its structure, pre-processing steps, and unique characteristics critical for understanding the context and experimental results. By offering this comprehensive view, we aim to enhance the clarity and reproducibility of our work.

9.1. DSEC-3DOD Dataset

The DSEC [20] dataset provides LiDAR, stereo RGB images, and stereo events from diverse driving scenarios. To date, the DSEC dataset has been extensively studied for 2D perception tasks (*e.g.* 2D object detection, semantic segmentation). In this study, we utilized this dataset for 3D perception for the first time and established the process of Fig. 8 to provide fine-grained 100 FPS 3D detection ground truth.

a. LiDAR-IMU SLAM

For 3D detection annotation, a LiDAR sensor providing accurate depth information was designated as the reference sensor. The odometry of the reference sensor was estimated to synchronize LiDAR data with image timestamps, enabling accurate inter-modality alignment. Manual labeling was performed on a dense point cloud generated through pose-based LiDAR accumulation. To ensure precise LiDAR pose estimation, the LIO-Mapping [112] method was employed, consistent with the approach utilized in the DSEC dataset. The poses for the 10 FPS LiDAR data were subsequently obtained.

b. Sequence Sampling

As mentioned in the main paper, we provide annotations for the “zurich_city” sequence. The DSEC provides images at 20 Hz and LiDAR data at 10 Hz. Images are sampled at 10 Hz following LiDAR. Although both the images and LiDAR data are sampled at the same 10 Hz rate, the lack of hardware time synchronization introduces temporal misalignment. To solve this problem, we utilize the sequence

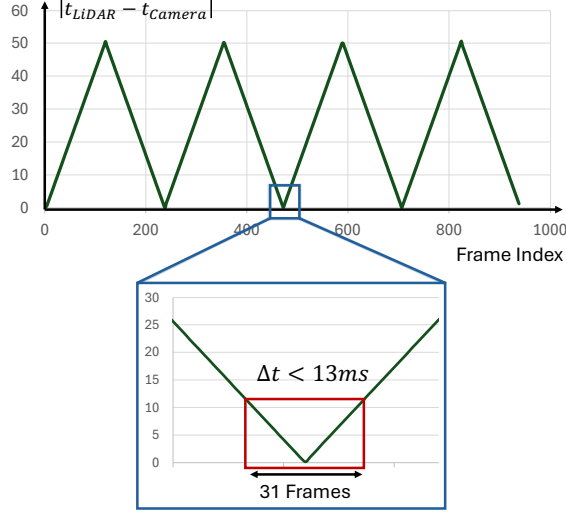


Figure 9. The time difference between images and closest LiDAR. To minimize temporal misalignment, 31 frames were sampled around the frame with the minimum time offset.

sampling strategy. Fig. 9 illustrates the absolute time difference between the nearest image and LiDAR frames. Due to the periodic discrepancy between the two sensors, this misalignment repeats approximately every 237 frames, with a maximum time offset of half a sensor period (*i.e.*, 50ms). Therefore, we sampled 31 frames centered around the point of minimal time offset, reducing the maximum misalignment of 13ms. As a result of sampling, the DSEC-3DOD dataset consists of 178 sequence chunks, each comprising 31 frames. Adjacent chunks are separated by a time gap of over 20 seconds, ensuring entirely different distributions in driving scenes. Table 9 and Table 10 show the train and test splits.

c. LiDAR-Image Synchronization

Although the sequence sampling was designed to minimize time misalignment, synchronization errors still persist. Therefore, we further aligned the LiDAR data to the image timestamps using pose-based adjustments.

For an arbitrary RGB image I_t at time t , the two closest-time LiDAR point clouds, P_{t_0} and P_{t_1} , are identified, where $t_0 < t < t_1$. Assume the corresponding poses X_{t_0} and X_{t_1} are available from the mapping of Process a. Each pose is represented as a 3D coordinate and quaternion, denoted as $X = (x, y, z, Q)$, where $Q \in \mathbb{R}^4$. The image-aligned LiDAR pose X_t is computed by interpolating X_{t_0} and X_{t_1} . The position is interpolated linearly, while spherical linear interpolation (SLERP) [89] is applied for the quaternions.

The synchronized LiDAR point cloud P_t is obtained using the transformation $P_t = T_t^{-1}T_{t'}P_{t'}$, where T_t and $T_{t'}$ are transformation matrices corresponding to the poses X_t

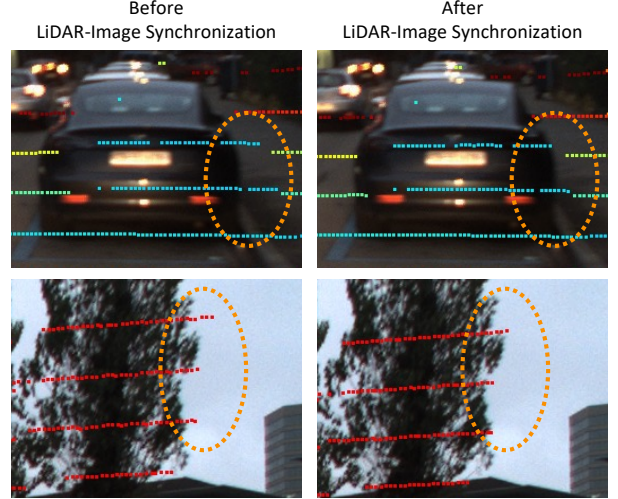


Figure 10. LiDAR projection on images before pose-based LiDAR synchronization (left) and after synchronization (right).

and $X_{t'}$, respectively. Here, t' is the nearest time to t as,

$$t' = \begin{cases} t_0 & \text{if } |t - t_0| < |t - t_1|, \\ t_1 & \text{otherwise.} \end{cases} \quad (4)$$

The effect of pose-based LiDAR synchronization is demonstrated in Fig. 10. LiDAR-image misalignment due to time offsets is most evident in scenes with large motions or significant rotations. By transforming the nearest LiDAR point cloud to the pose of the image timestamp, projection errors between sensors caused by time misalignment were minimized.

d. Point Cloud Densification

Raw LiDAR data is inherently sparse, which can lead to reduced accuracy in ground truth bounding boxes if used directly for annotation. To address this, we utilized an accumulated point cloud created by combining multiple LiDAR scans with their relative poses. As noted in the DSEC [20], LiDAR accumulation does not effectively handle occlusions or moving objects, both of which are critical considerations in the labeling process. To mitigate these issues, we employed filtered results (*i.e.*, disparity) during the annotation process.

e. Manual Annotation

Annotation experts labeled 3D bounding boxes on the densified 10 FPS LiDAR data, ensuring accuracy by considering both the LiDAR data and images. The ground truth consists of three classes: vehicle, pedestrian, and cyclist. Detailed annotation rules were derived from the guidelines provided by the Waymo Open Dataset [93]. To maintain high-quality annotations, bounding boxes containing fewer than two points or positioned beyond 50 meters were excluded from the ground truth.

f. Annotation Interpolation

To generate 100 FPS annotations from the manually labeled

10 FPS annotations, bounding boxes were interpolated to create ground truth for blind times where neither LiDAR nor images were available. Linear interpolation was applied to the bounding box pose and size, while SLERP interpolation was applied for rotations. The interpolated annotations were subsequently refined through the following process.

g. Sensor Data Interpolation

In process **f**, the automatically interpolated annotations are generally accurate but may not fully capture the dynamics of real-world motion. To enhance the quality of these annotations, sensor data was generated for the blind times. For images, realistic video frames were produced using a recent event-based video frame interpolation method [37]. Similarly, the latest techniques [125] were utilized to generate accurate and realistic intermediate point cloud data.

h. Annotation Filter and Refinement

The interpolated sensor data was employed to refine the annotations for the blind times. In most cases with minimal motion, bounding box interpolation alone yielded ground truth that aligned well with the sensor data. In such instances, refinements were avoided to preserve smooth bounding box poses and ensure temporal consistency. However, if the interpolated labels were misaligned with the sensor data or if sensor data was unavailable, the affected labels were filtered out.

9.2. Ev-Waymo Dataset

Event Synthesis. The Waymo Open Dataset (WOD) provides 10 FPS synchronized images, LiDAR, and 3D bounding box labels. To generate the events, we utilize a widely adopted event simulation model [18] to synthesize the events from video data. This enables us to utilize temporally dense events between image and LiDAR active timestamps for training and testing.

Annotation Interpolation and Refinement. Since WOD provides dense 10 FPS annotations, we can obtain 100 FPS ground truth through annotation interpolation and refinement. A process similar to the **f**, **g**, and **h** steps in DSEC-3DOD dataset processing was employed. We interpolated the 10 FPS bounding box information, including pose, dimensions, and heading, provided by WOD to generate 100 FPS data. In addition, we synthesized blind-time data of camera and LiDAR using an interpolation algorithm for refinement and filtering, ensuring higher quality.

10. More Qualitative Results and Videos

To provide a more comprehensive understanding of the proposed model, we present additional qualitative results in Figures 11, 12, and 13, showcasing its performance on the DSEC-3DOD dataset. The proposed method consistently predicts bounding boxes that closely align with the ground truth across various challenging environments.

Table 7. The result according to hyper-paramter in Eq. (3) on Ev-Waymo LEVEL 2 (L2). λ_1 and λ_2 refer to the weight of box regression loss and binary cross entropy loss, respectively.

$\lambda_1 \setminus \lambda_2$	0.1		1.0		10.0	
	mAP	mAPH	mAP	mAPH	mAP	mAPH
0.1	47.32	44.87	47.70	45.22	47.14	44.70
1.0	47.72	45.25	48.06	45.60	46.98	44.53
10.0	47.46	45.02	47.20	44.74	47.32	44.86

Figure 11 illustrates a challenging scene involving a bus, where size estimation is particularly difficult. The offline method, even with access to future information, fails to detect certain instances. Likewise, the online method demonstrates increasing errors compared to the ground truth as time progresses beyond the active timestamp. In contrast, the proposed method shows robust performance, generating predictions that closely align with the ground truth labels.

The introduced DSEC-3DOD dataset features challenging scenarios, including night scenes, as shown in Fig. 12. Unlike the Ev-Waymo dataset, which cannot leverage challenging illumination conditions to generate synthetic events, our proposed real event dataset enables validation in such scenarios. In the night scene, the proposed method exhibits accurate box predictions compared to both the offline and online methods.

Figure 14, 15, and 16 present the results on the Ev-Waymo dataset, which features numerous complex sequences with high object density. The proposed model effectively predicts complex object motions, producing bounding boxes closely aligned with the ground truth. In such scenes, even with access to future data, interpolating sensor information during blind times remains challenging, which complicates precise bounding box predictions. Consequently, the qualitative results on Ev-Waymo demonstrate that the proposed method outperforms others by delivering more accurate bounding boxes.

We provide a short video to showcase the datasets used in the experiments and the results on sequential data. The proposed method demonstrates robust performance across various environments in both the DSEC-3DOD dataset and the Ev-Waymo dataset. Notably, it accurately estimates the motion of object bounding boxes even in challenging night scenes within the DSEC-3DOD dataset.

11. Hyper-parameter Analysis

As shown in Table 7, we conduct an ablation study on the loss weights. The box regression loss and confidence prediction loss weights were set to 0.1, 1.0, and 10.0, respectively, during model training. The results demonstrated that the model remained robust, producing consistent outcomes despite changes in the loss magnitudes.

References

- [1] Xuyang Bai, Zeyu Hu, Xinge Zhu, Qingqiu Huang, Yilun Chen, Hongbo Fu, and Chiew-Lan Tai. Transfusion: Robust lidar-camera fusion for 3d object detection with transformers. In *Proceedings of the IEEE/CVF conference on computer vision and pattern recognition*, pages 1090–1099, 2022. 2
- [2] Yin Bi, Aaron Chadha, Alhabib Abbas, Eirina Bourtsoulatz, and Yiannis Andreopoulos. Graph-based object classification for neuromorphic vision sensing. *2019 IEEE/CVF International Conference on Computer Vision (ICCV)*, pages 491–501, 2019. 3
- [3] Xiaozhi Chen, Huimin Ma, Ji Wan, Bo Li, and Tian Xia. Multi-view 3d object detection network for autonomous driving. In *Proceedings of the IEEE conference on Computer Vision and Pattern Recognition*, pages 1907–1915, 2017. 2
- [4] Xuesong Chen, Shaoshuai Shi, Benjin Zhu, Ka Chun Cheung, Hang Xu, and Hongsheng Li. Mppnet: Multi-frame feature intertwining with proxy points for 3d temporal object detection. In *European Conference on Computer Vision*, pages 680–697. Springer, 2022. 2
- [5] Xuanyao Chen, Tianyuan Zhang, Yue Wang, Yilun Wang, and Hang Zhao. Futr3d: A unified sensor fusion framework for 3d detection. *2023 IEEE/CVF Conference on Computer Vision and Pattern Recognition Workshops (CVPRW)*, pages 172–181, 2022. 2
- [6] Yilun Chen, Shu Liu, Xiaoyong Shen, and Jiaya Jia. Fast point r-cnn. In *Proceedings of the IEEE/CVF international conference on computer vision*, pages 9775–9784, 2019. 2
- [7] Yilun Chen, Shu Liu, Xiaoyong Shen, and Jiaya Jia. Dsgn: Deep stereo geometry network for 3d object detection. In *Proceedings of the IEEE/CVF conference on computer vision and pattern recognition*, pages 12536–12545, 2020. 2
- [8] Yukang Chen, Yanwei Li, Xiangyu Zhang, Jian Sun, and Jiaya Jia. Focal sparse convolutional networks for 3d object detection. In *Proceedings of the IEEE/CVF Conference on Computer Vision and Pattern Recognition*, pages 5428–5437, 2022. 6, 7, 1
- [9] Yukang Chen, Jianhui Liu, Xiangyu Zhang, Xiaojuan Qi, and Jiaya Jia. Voxelnex: Fully sparse voxelnet for 3d object detection and tracking. In *Proceedings of the IEEE/CVF Conference on Computer Vision and Pattern Recognition*, pages 21674–21683, 2023. 6, 7, 1
- [10] Yi-Nan Chen, Hang Dai, and Yong Ding. Pseudo-stereo for monocular 3d object detection in autonomous driving. In *Proceedings of the IEEE/CVF conference on computer vision and pattern recognition*, pages 887–897, 2022. 2
- [11] Zehui Chen, Zhenyu Li, Shiquan Zhang, Liangji Fang, Qin-hong Jiang, and Feng Zhao. Deformable feature aggregation for dynamic multi-modal 3d object detection. In *European conference on computer vision*, pages 628–644. Springer, 2022. 2
- [12] Jiajun Deng, Shaoshuai Shi, Peiwei Li, Wengang Zhou, Yanyong Zhang, and Houqiang Li. Voxel r-cnn: Towards high performance voxel-based 3d object detection. In *Proceedings of the AAAI conference on artificial intelligence*, pages 1201–1209, 2021. 2, 4
- [13] Lue Fan, Ziqi Pang, Tianyuan Zhang, Yu-Xiong Wang, Hang Zhao, Feng Wang, Naiyan Wang, and Zhaoxiang Zhang. Embracing single stride 3d object detector with sparse transformer. In *Proceedings of the IEEE/CVF conference on computer vision and pattern recognition*, pages 8458–8468, 2022. 2
- [14] Tuo Feng, Ruijie Quan, Xiaohan Wang, Wenguan Wang, and Yi Yang. Interpretable3d: An ad-hoc interpretable classifier for 3d point clouds. In *Proceedings of the AAAI Conference on Artificial Intelligence*, pages 1761–1769, 2024. 2
- [15] Guillermo Gallego, Tobi Delbrück, Garrick Orchard, Chiara Bartolozzi, Brian Taba, Andrea Censi, Stefan Leutenegger, Andrew J Davison, Jörg Conradt, Kostas Daniilidis, et al. Event-based vision: A survey. *IEEE transactions on pattern analysis and machine intelligence*, 44 (1):154–180, 2020. 1
- [16] Daniel Gehrig and Davide Scaramuzza. Pushing the limits of asynchronous graph-based object detection with event cameras. *ArXiv*, abs/2211.12324, 2022. 3
- [17] Daniel Gehrig and Davide Scaramuzza. Low-latency automotive vision with event cameras. *Nature*, 629:1034 – 1040, 2024. 3
- [18] Daniel Gehrig, Mathias Gehrig, Javier Hidalgo-Carrió, and Davide Scaramuzza. Video to events: Recycling video datasets for event cameras. In *IEEE Conf. Comput. Vis. Pattern Recog. (CVPR)*, 2020. 5, 4
- [19] Mathias Gehrig and Davide Scaramuzza. Recurrent vision transformers for object detection with event cameras. *2023 IEEE/CVF Conference on Computer Vision and Pattern Recognition (CVPR)*, pages 13884–13893, 2022. 2, 3, 1
- [20] Mathias Gehrig, Willem Aarents, Daniel Gehrig, and Davide Scaramuzza. Dsec: A stereo event camera dataset for driving scenarios. *IEEE Robotics and Automation Letters*, 6(3):4947–4954, 2021. 5, 2, 3
- [21] Mathias Gehrig, Manasi Muglikar, and Davide Scaramuzza. Dense continuous-time optical flow from event cameras. *IEEE Transactions on Pattern Analysis and Machine Intelligence*, 2024. 2
- [22] Andreas Geiger, Philip Lenz, and Raquel Urtasun. Are we ready for autonomous driving? the kitti vision benchmark suite. *2012 IEEE Conference on Computer Vision and Pattern Recognition*, pages 3354–3361, 2012. 1
- [23] Tianrui Guan, Jun Wang, Shiyi Lan, Rohan Chandra, Zuxuan Wu, Larry Davis, and Dinesh Manocha. M3detr: Multi-representation, multi-scale, mutual-relation 3d object detection with transformers. In *Proceedings of the IEEE/CVF winter conference on applications of computer vision*, pages 772–782, 2022. 2
- [24] Xiaoyang Guo, Shaoshuai Shi, Xiaogang Wang, and Hongsheng Li. Liga-stereo: Learning lidar geometry aware representations for stereo-based 3d detector. In *Proceedings of the IEEE/CVF international conference on computer vision*, pages 3153–3163, 2021. 2

- [25] Ryuhei Hamaguchi, Yasutaka Furukawa, Masaki Onishi, and Ken Sakurada. Hierarchical neural memory network for low latency event processing. *2023 IEEE/CVF Conference on Computer Vision and Pattern Recognition (CVPR)*, pages 22867–22876, 2023. 3
- [26] Chenhong He, Hui Zeng, Jianqiang Huang, Xian-Sheng Hua, and Lei Zhang. Structure aware single-stage 3d object detection from point cloud. In *Proceedings of the IEEE/CVF conference on computer vision and pattern recognition*, pages 11873–11882, 2020. 2
- [27] Chenhong He, Ruihuang Li, Shuai Li, and Lei Zhang. Voxel set transformer: A set-to-set approach to 3d object detection from point clouds. In *Proceedings of the IEEE/CVF conference on computer vision and pattern recognition*, pages 8417–8427, 2022. 2
- [28] Tong He and Stefano Soatto. Mono3d++: Monocular 3d vehicle detection with two-scale 3d hypotheses and task priors. In *Proceedings of the AAAI Conference on Artificial Intelligence*, pages 8409–8416, 2019. 2
- [29] Cheng-Ju Ho, Chen-Hsuan Tai, Yen-Yu Lin, Ming-Hsuan Yang, and Yi-Hsuan Tsai. Diffusion-ss3d: Diffusion model for semi-supervised 3d object detection. *Advances in Neural Information Processing Systems*, 36:49100–49112, 2023. 2
- [30] Jordan SK Hu, Tianshu Kuai, and Steven L Waslander. Point density-aware voxels for lidar 3d object detection. In *Proceedings of the IEEE/CVF conference on computer vision and pattern recognition*, pages 8469–8478, 2022. 2, 4
- [31] Junjie Huang, Guan Huang, Zheng Zhu, Yun Ye, and Dalong Du. Bevdet: High-performance multi-camera 3d object detection in bird-eye-view. *arXiv preprint arXiv:2112.11790*, 2021. 2
- [32] Junjie Huang, Yun Ye, Zhuji Liang, Yi Shan, and Dalong Du. Detecting as labeling: Rethinking lidar-camera fusion in 3d object detection. In *European Conference on Computer Vision*, pages 439–455. Springer, 2025. 2
- [33] Kuan-Chih Huang, Tsung-Han Wu, Hung-Ting Su, and Winston H Hsu. Monodtr: Monocular 3d object detection with depth-aware transformer. In *Proceedings of the IEEE/CVF conference on computer vision and pattern recognition*, pages 4012–4021, 2022. 2
- [34] Yu Huang, Chenzhuang Du, Zihui Xue, Xuanyao Chen, Hang Zhao, and Longbo Huang. What makes multi-modal learning better than single (provably). *Advances in Neural Information Processing Systems*, 34:10944–10956, 2021. 2
- [35] Massimiliano Iacono, Stefan Weber, Arren J. Glover, and Chiara Bartolozzi. Towards event-driven object detection with off-the-shelf deep learning. *2018 IEEE/RSJ International Conference on Intelligent Robots and Systems (IROS)*, pages 1–9, 2018. 3
- [36] Yanqin Jiang, Li Zhang, Zhenwei Miao, Xiatian Zhu, Jin Gao, Weiming Hu, and Yu-Gang Jiang. Polarformer: Multi-camera 3d object detection with polar transformer. In *Proceedings of the AAAI conference on Artificial Intelligence*, pages 1042–1050, 2023. 2
- [37] Taewoo Kim, Yujeong Chae, Hyun-Kurl Jang, and Kuk-Jin Yoon. Event-based video frame interpolation with cross-modal asymmetric bidirectional motion fields. In *Proceedings of the IEEE/CVF Conference on Computer Vision and Pattern Recognition*, pages 18032–18042, 2023. 5, 6, 7, 4, 12, 13, 14
- [38] Taewoo Kim, Hoonhee Cho, and Kuk-Jin Yoon. Cross-modal temporal alignment for event-guided video deblurring. *arXiv preprint arXiv:2408.14930*, 2024. 2
- [39] Diederik P Kingma. Adam: A method for stochastic optimization. *arXiv preprint arXiv:1412.6980*, 2014. 1
- [40] Jason Ku, Melissa Mozifian, Jungwook Lee, Ali Harakeh, and Steven L Waslander. Joint 3d proposal generation and object detection from view aggregation. In *2018 IEEE/RSJ International Conference on Intelligent Robots and Systems (IROS)*, pages 1–8. IEEE, 2018. 2
- [41] Alex H Lang, Sourabh Vora, Holger Caesar, Lubing Zhou, Jiong Yang, and Oscar Beijbom. Pointpillars: Fast encoders for object detection from point clouds. In *Proceedings of the IEEE/CVF conference on computer vision and pattern recognition*, pages 12697–12705, 2019. 2
- [42] Dianze Li, Jianing Li, and Yonghong Tian. Sodformer: Streaming object detection with transformer using events and frames. *IEEE Transactions on Pattern Analysis and Machine Intelligence*, 45:14020–14037, 2023. 3
- [43] Jianing Li, Jia Li, Lin Zhu, Xijie Xiang, Tiejun Huang, and Yonghong Tian. Asynchronous spatio-temporal memory network for continuous event-based object detection. *IEEE Transactions on Image Processing*, 31:2975–2987, 2022. 3
- [44] Peiliang Li, Xiaozhi Chen, and Shaojie Shen. Stereo r-cnn based 3d object detection for autonomous driving. In *Proceedings of the IEEE/CVF Conference on Computer Vision and Pattern Recognition*, pages 7644–7652, 2019. 2
- [45] Xin Li, Tao Ma, Yuenan Hou, Botian Shi, Yuchen Yang, Youquan Liu, Xingjiao Wu, Qin Chen, Yikang Li, Yu Qiao, et al. Logonet: Towards accurate 3d object detection with local-to-global cross-modal fusion. In *Proceedings of the IEEE/CVF Conference on Computer Vision and Pattern Recognition*, pages 17524–17534, 2023. 2, 3, 5, 6, 7, 1
- [46] Xiaotian Li, Baojie Fan, Jiandong Tian, and Huijie Fan. Gafusion: Adaptive fusing lidar and camera with multiple guidance for 3d object detection. In *Proceedings of the IEEE/CVF Conference on Computer Vision and Pattern Recognition*, pages 21209–21218, 2024. 2
- [47] Xiang Li, Junbo Yin, Wei Li, Chengzhong Xu, Ruigang Yang, and Jianbing Shen. Di-v2x: Learning domain-invariant representation for vehicle-infrastructure collaborative 3d object detection. In *Proceedings of the AAAI Conference on Artificial Intelligence*, pages 3208–3215, 2024. 2
- [48] Yijin Li, Han Zhou, Bangbang Yang, Yexin Zhang, Zhaopeng Cui, Hujun Bao, and Guofeng Zhang. Graph-based asynchronous event processing for rapid object recognition. *2021 IEEE/CVF International Conference on Computer Vision (ICCV)*, pages 914–923, 2021. 3
- [49] Yanwei Li, Yilun Chen, Xiaojuan Qi, Zeming Li, Jian Sun, and Jiaya Jia. Unifying voxel-based representation with transformer for 3d object detection. *Advances in Neural Information Processing Systems*, 35:18442–18455, 2022. 2

- [50] Yanwei Li, Xiaojuan Qi, Yukang Chen, Liwei Wang, Zeming Li, Jian Sun, and Jiaya Jia. Voxel field fusion for 3d object detection. In *Proceedings of the IEEE/CVF Conference on Computer Vision and Pattern Recognition*, pages 1120–1129, 2022.
- [51] Yingwei Li, Adams Wei Yu, Tianjian Meng, Ben Caine, Jiquan Ngiam, Daiyi Peng, Junyang Shen, Yifeng Lu, Denny Zhou, Quoc V Le, et al. Deepfusion: Lidar-camera deep fusion for multi-modal 3d object detection. In *Proceedings of the IEEE/CVF conference on computer vision and pattern recognition*, pages 17182–17191, 2022. 2
- [52] Yinhao Li, Zheng Ge, Guanyi Yu, Jinrong Yang, Zengran Wang, Yukang Shi, Jianjian Sun, and Zeming Li. Bevdepth: Acquisition of reliable depth for multi-view 3d object detection. In *Proceedings of the AAAI Conference on Artificial Intelligence*, pages 1477–1485, 2023. 2
- [53] Zhichao Li, Feng Wang, and Naiyan Wang. Lidar r-cnn: An efficient and universal 3d object detector. In *Proceedings of the IEEE/CVF conference on computer vision and pattern recognition*, pages 7546–7555, 2021. 2
- [54] Ming Liang, Bin Yang, Shenlong Wang, and Raquel Urtasun. Deep continuous fusion for multi-sensor 3d object detection. In *Proceedings of the European conference on computer vision (ECCV)*, pages 641–656, 2018. 2
- [55] Ming Liang, Bin Yang, Yun Chen, Rui Hu, and Raquel Urtasun. Multi-task multi-sensor fusion for 3d object detection. In *Proceedings of the IEEE/CVF conference on computer vision and pattern recognition*, pages 7345–7353, 2019. 2
- [56] Tingting Liang, Hongwei Xie, Kaicheng Yu, Zhongyu Xia, Zhiwei Lin, Yongtao Wang, Tao Tang, Bing Wang, and Zhi Tang. Bevfusion: A simple and robust lidar-camera fusion framework. *Advances in Neural Information Processing Systems*, 35:10421–10434, 2022. 2
- [57] Zhiwei Lin, Zhe Liu, Zhongyu Xia, Xinhao Wang, Yongtao Wang, Shengxiang Qi, Yang Dong, Nan Dong, Le Zhang, and Ce Zhu. Rcbvdet: Radar-camera fusion in bird’s eye view for 3d object detection. In *Proceedings of the IEEE/CVF Conference on Computer Vision and Pattern Recognition*, pages 14928–14937, 2024. 2
- [58] Xianpeng Liu, Ce Zheng, Ming Qian, Nan Xue, Chen Chen, Zhebin Zhang, Chen Li, and Tianfu Wu. Multi-view attentive contextualization for multi-view 3d object detection. In *Proceedings of the IEEE/CVF Conference on Computer Vision and Pattern Recognition (CVPR)*, pages 16688–16698, 2024. 2
- [59] Yingfei Liu, Tiancai Wang, Xiangyu Zhang, and Jian Sun. Petr: Position embedding transformation for multi-view 3d object detection. In *European Conference on Computer Vision*, pages 531–548. Springer, 2022.
- [60] Zechen Liu, Zizhang Wu, and Roland Tóth. Smoke: Single-stage monocular 3d object detection via keypoint estimation. In *Proceedings of the IEEE/CVF conference on computer vision and pattern recognition workshops*, pages 996–997, 2020. 2
- [61] Ze Liu, Yutong Lin, Yue Cao, Han Hu, Yixuan Wei, Zheng Zhang, Stephen Lin, and Baining Guo. Swin transformer: Hierarchical vision transformer using shifted windows. *2021 IEEE/CVF International Conference on Computer Vision (ICCV)*, pages 9992–10002, 2021. 1
- [62] Zhijian Liu, Haotian Tang, Alexander Amini, Xinyu Yang, Huizi Mao, Daniela L Rus, and Song Han. Bevfusion: Multi-task multi-sensor fusion with unified bird’s-eye view representation. In *2023 IEEE international conference on robotics and automation (ICRA)*, pages 2774–2781. IEEE, 2023. 2
- [63] Yan Lu, Xinzhu Ma, Lei Yang, Tianzhu Zhang, Yating Liu, Qi Chu, Junjie Yan, and Wanli Ouyang. Geometry uncertainty projection network for monocular 3d object detection. In *Proceedings of the IEEE/CVF International Conference on Computer Vision*, pages 3111–3121, 2021. 2
- [64] Jiageng Mao, Minzhe Niu, Haoyue Bai, Xiaodan Liang, Hang Xu, and Chunjing Xu. Pyramid r-cnn: Towards better performance and adaptability for 3d object detection. In *Proceedings of the IEEE/CVF International Conference on Computer Vision*, pages 2723–2732, 2021. 2
- [65] Jiageng Mao, Yujing Xue, Minzhe Niu, Haoyue Bai, Jiaoshi Feng, Xiaodan Liang, Hang Xu, and Chunjing Xu. Voxel transformer for 3d object detection. In *Proceedings of the IEEE/CVF international conference on computer vision*, pages 3164–3173, 2021. 2
- [66] Nico Messikommer, Daniel Gehrig, Antonio Loquercio, and Davide Scaramuzza. Event-based asynchronous sparse convolutional networks. *ArXiv*, abs/2003.09148, 2020. 3
- [67] Zhenwei Miao, Jikai Chen, Hongyu Pan, Ruiwen Zhang, Kaixuan Liu, Peihan Hao, Jun Zhu, Yang Wang, and Xin Zhan. Pvgnet: A bottom-up one-stage 3d object detector with integrated multi-level features. In *Proceedings of the IEEE/CVF Conference on Computer Vision and Pattern Recognition*, pages 3279–3288, 2021. 2
- [68] Su Pang, Daniel Morris, and Hayder Radha. Cloccs: Camera-lidar object candidates fusion for 3d object detection. In *2020 IEEE/RSJ International Conference on Intelligent Robots and Systems (IROS)*, pages 10386–10393. IEEE, 2020. 2
- [69] Dennis Park, Rares Ambrus, Vitor Guizilini, Jie Li, and Adrien Gaidon. Is pseudo-lidar needed for monocular 3d object detection? In *Proceedings of the IEEE/CVF International Conference on Computer Vision*, pages 3142–3152, 2021. 2
- [70] Wanli Peng, Hao Pan, He Liu, and Yi Sun. Ida-3d: Instance-depth-aware 3d object detection from stereo vision for autonomous driving. In *Proceedings of the IEEE/CVF conference on computer vision and pattern recognition*, pages 13015–13024, 2020. 2
- [71] Yan Peng, Yueyi Zhang, Peilin Xiao, Xiaoyan Sun, and Feng Wu. Better and faster: Adaptive event conversion for event-based object detection. In *AAAI Conference on Artificial Intelligence*, 2023. 3
- [72] Yansong Peng, Yueyi Zhang, Zhiwei Xiong, Xiaoyan Sun, and Feng Wu. Get: Group event transformer for event-based vision. *2023 IEEE/CVF International Conference on Computer Vision (ICCV)*, pages 6015–6025, 2023. 3
- [73] Yansong Peng, Hebei Li, Yueyi Zhang, Xiaoyan Sun, and Feng Wu. Scene adaptive sparse transformer for event-

based object detection. *2024 IEEE/CVF Conference on Computer Vision and Pattern Recognition (CVPR)*, pages 16794–16804, 2024. 3

- [74] Etienne Perot, Pierre de Tournemire, Davide Oscar Nitti, Jonathan Masci, and Amos Sironi. Learning to detect objects with a 1 megapixel event camera. *ArXiv*, abs/2009.13436, 2020. 3
- [75] Jonah Philion and Sanja Fidler. Lift, splat, shoot: Encoding images from arbitrary camera rigs by implicitly unprojecting to 3d. In *Computer Vision–ECCV 2020: 16th European Conference, Glasgow, UK, August 23–28, 2020, Proceedings, Part XIV 16*, pages 194–210. Springer, 2020. 2
- [76] AJ Piergiovanni, Vincent Casser, Michael S Ryoo, and Anelia Angelova. 4d-net for learned multi-modal alignment. In *Proceedings of the IEEE/CVF International Conference on Computer Vision*, pages 15435–15445, 2021. 2
- [77] Aditya Prakash, Kashyap Chitta, and Andreas Geiger. Multi-modal fusion transformer for end-to-end autonomous driving. In *Proceedings of the IEEE/CVF conference on computer vision and pattern recognition*, pages 7077–7087, 2021. 2
- [78] Charles R Qi, Hao Su, Kaichun Mo, and Leonidas J Guibas. Pointnet: Deep learning on point sets for 3d classification and segmentation. In *Proceedings of the IEEE conference on computer vision and pattern recognition*, pages 652–660, 2017. 2
- [79] Charles Ruizhongtai Qi, Li Yi, Hao Su, and Leonidas J Guibas. Pointnet++: Deep hierarchical feature learning on point sets in a metric space. *Advances in neural information processing systems*, 30, 2017. 2
- [80] Charles R Qi, Wei Liu, Chenxia Wu, Hao Su, and Leonidas J Guibas. Frustum pointnets for 3d object detection from rgb-d data. In *Proceedings of the IEEE conference on computer vision and pattern recognition*, pages 918–927, 2018. 2
- [81] Charles R Qi, Or Litany, Kaiming He, and Leonidas J Guibas. Deep hough voting for 3d object detection in point clouds. In *proceedings of the IEEE/CVF International Conference on Computer Vision*, pages 9277–9286, 2019. 2
- [82] Cody Reading, Ali Harakeh, Julia Chae, and Steven L Waslander. Categorical depth distribution network for monocular 3d object detection. In *Proceedings of the IEEE/CVF Conference on Computer Vision and Pattern Recognition*, pages 8555–8564, 2021. 2
- [83] Simon Schaefer, Daniel Gehrig, and Davide Scaramuzza. Aegnn: Asynchronous event-based graph neural networks. In *IEEE Conference on Computer Vision and Pattern Recognition*, 2022. 3
- [84] Hualian Sheng, Sijia Cai, Yuan Liu, Bing Deng, Jianqiang Huang, Xian-Sheng Hua, and Min-Jian Zhao. Improving 3d object detection with channel-wise transformer. In *Proceedings of the IEEE/CVF international conference on computer vision*, pages 2743–2752, 2021. 2
- [85] Shaoshuai Shi, Xiaogang Wang, and Hongsheng Li. Pointr-cnn: 3d object proposal generation and detection from point cloud. In *Proceedings of the IEEE/CVF conference on computer vision and pattern recognition*, pages 770–779, 2019. 2
- [86] Shaoshuai Shi, Chaoxu Guo, Li Jiang, Zhe Wang, Jianping Shi, Xiaogang Wang, and Hongsheng Li. Pv-rcnn: Point-voxel feature set abstraction for 3d object detection. In *Proceedings of the IEEE/CVF conference on computer vision and pattern recognition*, pages 10529–10538, 2020. 2
- [87] Weijing Shi and Raj Rajkumar. Point-gnn: Graph neural network for 3d object detection in a point cloud. In *Proceedings of the IEEE/CVF conference on computer vision and pattern recognition*, pages 1711–1719, 2020. 2
- [88] Shintaro Shiba, Yoshimitsu Aoki, and Guillermo Gallego. Secrets of event-based optical flow. In *European Conference on Computer Vision*, pages 628–645. Springer, 2022. 2
- [89] Ken Shoemake. Animating rotation with quaternion curves. *Proceedings of the 12th annual conference on Computer graphics and interactive techniques*, 1985. 3
- [90] Leslie N Smith and Nicholay Topin. Super-convergence: Very fast training of neural networks using large learning rates. In *Artificial intelligence and machine learning for multi-domain operations applications*, pages 369–386. SPIE, 2019. 1
- [91] Ziyang Song, Lei Yang, Shaoqing Xu, Lin Liu, Dongyang Xu, Caiyan Jia, Feiyang Jia, and Li Wang. Graphbev: Towards robust bev feature alignment for multi-modal 3d object detection. *arXiv preprint arXiv:2403.11848*, 2024. 2
- [92] Jiaming Sun, Linghao Chen, Yiming Xie, Siyu Zhang, Qin-hong Jiang, Xiaowei Zhou, and Hujun Bao. Disp r-cnn: Stereo 3d object detection via shape prior guided instance disparity estimation. In *Proceedings of the IEEE/CVF conference on computer vision and pattern recognition*, pages 10548–10557, 2020. 2
- [93] Pei Sun, Henrik Kretzschmar, Xerxes Dotiwalla, Aurelien Chouard, Vijaysai Patnaik, Paul Tsui, James Guo, Yin Zhou, Yuning Chai, Benjamin Caine, Vijay Vasudevan, Wei Han, Jiquan Ngiam, Hang Zhao, Aleksei Timofeev, Scott M. Ettinger, Maxim Krivokon, Amy Gao, Aditya Joshi, Yu Zhang, Jonathon Shlens, Zhifeng Chen, and Dragomir Anguelov. Scalability in perception for autonomous driving: Waymo open dataset. *2020 IEEE/CVF Conference on Computer Vision and Pattern Recognition (CVPR)*, pages 2443–2451, 2019. 5, 3
- [94] Stepan Tulyakov, Alfredo Bochicchio, Daniel Gehrig, Stamatios Georgoulis, Yuanyou Li, and Davide Scaramuzza. Time lens++: Event-based frame interpolation with parametric non-linear flow and multi-scale fusion. In *Proceedings of the IEEE/CVF Conference on Computer Vision and Pattern Recognition*, pages 17755–17764, 2022. 2
- [95] Sourabh Vora, Alex H Lang, Bassam Helou, and Oscar Beijbom. Pointpainting: Sequential fusion for 3d object detection. In *Proceedings of the IEEE/CVF conference on computer vision and pattern recognition*, pages 4604–4612, 2020. 2
- [96] Zhexiong Wan, Yuxin Mao, Jing Zhang, and Yuchao Dai. Rpeflow: Multimodal fusion of rgb-pointcloud-event for joint optical flow and scene flow estimation. In *Proceedings of the IEEE/CVF International Conference on Computer Vision*, pages 10030–10040, 2023. 1

- [97] Dongsheng Wang, Xu Jia, Yang Zhang, Xinyu Zhang, Yaoyuan Wang, Ziyang Zhang, D. Wang, and Huchuan Lu. Dual memory aggregation network for event-based object detection with learnable representation. In *AAAI Conference on Artificial Intelligence*, 2023. 3
- [98] Wenjie Wang, Yehao Lu, Guangcong Zheng, Shuigen Zhan, Xiaoqing Ye, Zichang Tan, Jingdong Wang, Gaoang Wang, and Xi Li. Bevspread: Spread voxel pooling for bird’s-eye-view representation in vision-based roadside 3d object detection. In *Proceedings of the IEEE/CVF Conference on Computer Vision and Pattern Recognition*, pages 14718–14727, 2024. 2
- [99] Yan Wang, Wei-Lun Chao, Divyansh Garg, Bharath Hariharan, Mark Campbell, and Kilian Q Weinberger. Pseudo-lidar from visual depth estimation: Bridging the gap in 3d object detection for autonomous driving. In *Proceedings of the IEEE/CVF conference on computer vision and pattern recognition*, pages 8445–8453, 2019. 2
- [100] Yue Wang, Vitor Campagnolo Guizilini, Tianyuan Zhang, Yilun Wang, Hang Zhao, and Justin Solomon. Detr3d: 3d object detection from multi-view images via 3d-to-2d queries. In *Conference on Robot Learning*, pages 180–191. PMLR, 2022. 2
- [101] Yan Wang, Junbo Yin, Wei Li, Pascal Frossard, Ruigang Yang, and Jianbing Shen. Ssda3d: Semi-supervised domain adaptation for 3d object detection from point cloud. In *Proceedings of the AAAI Conference on Artificial Intelligence*, pages 2707–2715, 2023. 2
- [102] Yichen Xie, Chenfeng Xu, Marie-Julie Rakotosaona, Patrick Rim, Federico Tombari, Kurt Keutzer, Masayoshi Tomizuka, and Wei Zhan. Sparsefusion: Fusing multi-modal sparse representations for multi-sensor 3d object detection. *2023 IEEE/CVF International Conference on Computer Vision (ICCV)*, pages 17545–17556, 2023. 2
- [103] Danfei Xu, Dragomir Anguelov, and Ashesh Jain. Pointfusion: Deep sensor fusion for 3d bounding box estimation. In *Proceedings of the IEEE conference on computer vision and pattern recognition*, pages 244–253, 2018. 2
- [104] Jianyun Xu, Zhenwei Miao, Da Zhang, Hongyu Pan, Kaixuan Liu, Peihan Hao, Jun Zhu, Zhengyang Sun, Hongmin Li, and Xin Zhan. Int: Towards infinite-frames 3d detection with an efficient framework. In *European Conference on Computer Vision*, pages 193–209. Springer, 2022. 2
- [105] Shaoqing Xu, Dingfu Zhou, Jin Fang, Junbo Yin, Zhou Bin, and Liangjun Zhang. Fusionpainting: Multimodal fusion with adaptive attention for 3d object detection. In *2021 IEEE International Intelligent Transportation Systems Conference (ITSC)*, pages 3047–3054. IEEE, 2021. 2
- [106] Yan Yan, Yuxing Mao, and Bo Li. Second: Sparsely embedded convolutional detection. *Sensors (Basel, Switzerland)*, 18, 2018. 5
- [107] Yixin Yang, Jinxiu Liang, Bohan Yu, Yan Chen, Jimmy S Ren, and Boxin Shi. Latency correction for event-guided deblurring and frame interpolation. In *Proceedings of the IEEE/CVF Conference on Computer Vision and Pattern Recognition*, pages 24977–24986, 2024. 2
- [108] Zetong Yang, Yanan Sun, Shu Liu, Xiaoyong Shen, and Jiaya Jia. Std: Sparse-to-dense 3d object detector for point cloud. In *Proceedings of the IEEE/CVF international conference on computer vision*, pages 1951–1960, 2019. 2
- [109] Zetong Yang, Yanan Sun, Shu Liu, and Jiaya Jia. 3dssd: Point-based 3d single stage object detector. In *Proceedings of the IEEE/CVF conference on computer vision and pattern recognition*, pages 11040–11048, 2020. 2
- [110] Zeyu Yang, Jiaqi Chen, Zhenwei Miao, Wei Li, Xiatian Zhu, and Li Zhang. Deepinteraction: 3d object detection via modality interaction. *Advances in Neural Information Processing Systems*, 35:1992–2005, 2022. 2
- [111] Man Yao, Huanhuan Gao, Guangshe Zhao, Dingheng Wang, Yihan Lin, Zhao-Xu Yang, and Guoqi Li. Temporal-wise attention spiking neural networks for event streams classification. *2021 IEEE/CVF International Conference on Computer Vision (ICCV)*, pages 10201–10210, 2021. 3
- [112] Haoyang Ye, Yuying Chen, and Ming Liu. Tightly coupled 3d lidar inertial odometry and mapping. *2019 International Conference on Robotics and Automation (ICRA)*, pages 3144–3150, 2019. 2
- [113] Junbo Yin, Jin Fang, Dingfu Zhou, Liangjun Zhang, Cheng-Zhong Xu, Jianbing Shen, and Wenguan Wang. Semi-supervised 3d object detection with proficient teachers. In *European Conference on Computer Vision*, pages 727–743. Springer, 2022. 2
- [114] Junbo Yin, Dingfu Zhou, Liangjun Zhang, Jin Fang, Cheng-Zhong Xu, Jianbing Shen, and Wenguan Wang. Proposal-contrast: Unsupervised pre-training for lidar-based 3d object detection. In *European conference on computer vision*, pages 17–33. Springer, 2022. 2
- [115] Junbo Yin, Jianbing Shen, Runnan Chen, Wei Li, Ruigang Yang, Pascal Frossard, and Wenguan Wang. Is-fusion: Instance-scene collaborative fusion for multimodal 3d object detection. *2024 IEEE/CVF Conference on Computer Vision and Pattern Recognition (CVPR)*, pages 14905–14915, 2024. 1
- [116] Junbo Yin, Jianbing Shen, Runnan Chen, Wei Li, Ruigang Yang, Pascal Frossard, and Wenguan Wang. Is-fusion: Instance-scene collaborative fusion for multimodal 3d object detection. In *Proceedings of the IEEE/CVF Conference on Computer Vision and Pattern Recognition*, pages 14905–14915, 2024. 2
- [117] Tianwei Yin, Xingyi Zhou, and Philipp Krahenbuhl. Center-based 3d object detection and tracking. In *Proceedings of the IEEE/CVF conference on computer vision and pattern recognition*, pages 11784–11793, 2021. 3, 4, 5
- [118] Yurong You, Yan Wang, Wei-Lun Chao, Divyansh Garg, Geoff Pleiss, Bharath Hariharan, Mark Campbell, and Kilian Q Weinberger. Pseudo-lidar++: Accurate depth for 3d object detection in autonomous driving. *arXiv preprint arXiv:1906.06310*, 2019. 2
- [119] Guozhen Zhang, Yuhua Zhu, Haonan Wang, Youxin Chen, Gangshan Wu, and Limin Wang. Extracting motion and appearance via inter-frame attention for efficient video frame interpolation. In *Proceedings of the IEEE/CVF Conference on Computer Vision and Pattern Recognition*, pages 5682–5692, 2023. 6, 7
- [120] Gang Zhang, Junnan Chen, Guohuan Gao, Jianmin Li, Si Liu, and Xiaolin Hu. Safdnet: A simple and effective net-

- work for fully sparse 3d object detection. In *Proceedings of the IEEE/CVF Conference on Computer Vision and Pattern Recognition (CVPR)*, pages 14477–14486, 2024. [2](#)
- [121] Gang Zhang, Chen Junnan, Guohuan Gao, Jianmin Li, and Xiaolin Hu. Hednet: A hierarchical encoder-decoder network for 3d object detection in point clouds. *Advances in Neural Information Processing Systems*, 36, 2024. [6](#), [7](#), [1](#)
- [122] Jiqing Zhang, B. Dong, Haiwei Zhang, Jianchuan Ding, Felix Heide, Baocai Yin, and Xin Yang. Spiking transformers for event-based single object tracking. *2022 IEEE/CVF Conference on Computer Vision and Pattern Recognition (CVPR)*, pages 8791–8800, 2022. [3](#)
- [123] Renrui Zhang, Han Qiu, Tai Wang, Ziyu Guo, Ziteng Cui, Yu Qiao, Hongsheng Li, and Peng Gao. Monodetr: Depth-guided transformer for monocular 3d object detection. In *Proceedings of the IEEE/CVF International Conference on Computer Vision*, pages 9155–9166, 2023. [2](#)
- [124] Yanan Zhang, Jiaxin Chen, and Di Huang. Cat-det: Contrastively augmented transformer for multi-modal 3d object detection. In *Proceedings of the IEEE/CVF Conference on Computer Vision and Pattern Recognition*, pages 908–917, 2022. [2](#)
- [125] Zehan Zheng, Danni Wu, Ruisi Lu, Fan Lu, Guang Chen, and Changjun Jiang. Neuralpci: Spatio-temporal neural field for 3d point cloud multi-frame non-linear interpolation. In *Proceedings of the IEEE/CVF Conference on Computer Vision and Pattern Recognition*, pages 909–918, 2023. [5](#), [6](#), [7](#), [4](#)
- [126] Dingfu Zhou, Jin Fang, Xibin Song, Liu Liu, Junbo Yin, Yuchao Dai, Hongdong Li, and Ruigang Yang. Joint 3d instance segmentation and object detection for autonomous driving. In *Proceedings of the IEEE/CVF Conference on Computer Vision and Pattern Recognition*, pages 1839–1849, 2020. [2](#)
- [127] Hanyu Zhou, Yi Chang, and Zhiwei Shi. Bring event into rgb and lidar: Hierarchical visual-motion fusion for scene flow. In *Proceedings of the IEEE/CVF Conference on Computer Vision and Pattern Recognition*, pages 26477–26486, 2024. [1](#)
- [128] Yin Zhou and Oncel Tuzel. Voxelnet: End-to-end learning for point cloud based 3d object detection. In *Proceedings of the IEEE conference on computer vision and pattern recognition*, pages 4490–4499, 2018. [2](#), [3](#), [4](#), [1](#)
- [129] Alex Zihao Zhu, Liangzhe Yuan, Kenneth Chaney, and Kostas Daniilidis. Unsupervised event-based learning of optical flow, depth, and egomotion. In *Proceedings of the IEEE/CVF Conference on Computer Vision and Pattern Recognition*, pages 989–997, 2019. [3](#)
- [130] Nikola Zubic, Daniel Gehrig, Mathias Gehrig, and Davide Scaramuzza. From chaos comes order: Ordering event representations for object recognition and detection. *2023 IEEE/CVF International Conference on Computer Vision (ICCV)*, pages 12800–12810, 2023. [3](#)

Table 8. The train/test sequence splits of Ev-Waymo dataset.

Dataset	Ev-Waymo		
Split	Sequence Name	No. Seq.	No. Labeled Scenes
Train	segment-207754730878135627_1140_000_1160_000, segment-13840133134545942567_1060_000_1080_000, segment-8327447186504415549_5200_000_5220_000, segment-10964956617027590844_1584_680_1604_680, segment-11918003324473417938_1400_000_1420_000, segment-15448466074775525292_2920_000_2940_000, segment-14830022845193837364_3488_060_3508_060, segment-11379226583756500423_6230_810_6250_810, segment-7861168750216313148_1305_290_1325_290, segment-13506499849906169066_120_000_140_000, segment-6229371035421550389_2220_000_2240_000, segment-15882343134097151256_4820_000_4840_000, segment-14098605172844003779_5084_630_5104_630, segment-8582923946352460474_2360_000_2380_000, segment-16485056021060230344_1576_741_1596_741, segment-915935412356143375_1740_030_1760_030, segment-3002379261592154728_2256_691_2276_691, segment-4348478035380346090_1000_000_1020_000, segment-2036908808378190283_4340_000_4360_000, segment-15844593126368860820_3260_000_3280_000, segment-5835049423600303130_180_000_200_000, segment-15696964848687303249_4615_200_4635_200, segment-7543690094688232666_4945_350_4965_350, segment-16372013171456210875_5631_040_5651_040, segment-14193044537086402364_534_000_554_000, segment-550171902340535682_2640_000_2660_000, segment-4641822195449131669_380_000_400_000, segment-7239123081683545077_4044_370_4064_370, segment-11928449532664718059_1200_000_1220_000, segment-5100136784230856773_2517_300_2537_300, segment-13182548552824592684_4160_250_4180_250, segment-14004546003548947884_2331_861_2351_861, segment-2570264768774616538_860_000_880_000, segment-7440437175443450101_94_000_114_000, segment-15717839202171538526_1124_920_1144_920, segment-8148053503558757176_4240_000_4260_000, segment-16977844994272847523_2140_000_2160_000, segment-5451442719480728410_5660_000_5680_000, segment-7290499689576448085_3960_000_3980_000, segment-16801666784196221098_2480_000_2500_000, segment-4916527289027259239_5180_000_5200_000, segment-16202688197024602345_3818_820_3838_820, segment-9758342966297863572_875_230_895_230, segment-12161824480686739258_1813_380_1833_380, segment-14369250836076988112_7249_040_7269_040, segment-2752216004511723012_260_000_280_000, segment-10444454289801298640_4360_000_4380_000, segment-17388121177218499911_2520_000_2540_000, segment-7885161619764516373_289_280_309_280, segment-16561295363965082313_3720_000_3740_000, segment-11199484219241918646_2810_030_2830_030, segment-4575961016807404107_880_000_900_000, segment-7566697458525030390_1440_000_1460_000, segment-10275144660749673822_5755_561_5775_561, segment-6193696614129429757_2420_000_2440_000, segment-12251442326766052580_1840_000_1860_000, segment-13271285919570645382_5320_000_5340_000, segment-9015546800913584551_4431_180_4451_180, segment-10596949720463106554_1933_530_1953_530, segment-15942468615931009553_1243_190_1263_190, segment-15125792363972595336_4960_000_4980_000, segment-1422926405879888210_51_310_71_310, segment-5576800480528461086_1000_000_1020_000, segment-1255991971750044803_1700_000_1720_000	64	126,330
Test	segment-18446264979321894359_3700_000_3720_000, segment-17152649515605309595_3440_000_3460_000, segment-16213317953898915772_1597_170_1617_170, segment-5183174891274719570_3464_030_3484_030, segment-3126522626440597519_806_440_826_440, segment-3077229433993844199_1080_000_1100_000, segment-10289507859301986274_4200_000_4220_000, segment-30779396576054160_1880_000_1900_000, segment-9243656068381062947_1297_428_1317_428, segment-2834723872140855871_1615_000_1635_000, segment-2736377008667623133_2676_410_2696_410, segment-15948509588157321530_7187_290_7207_290, segment-9231652062943496183_1740_000_1760_000, segment-4854173791890687260_2880_000_2900_000, segment-6324079979569135086_2372_300_2392_300, segment-6001094526418694294_4609_470_4629_470	16	31,550

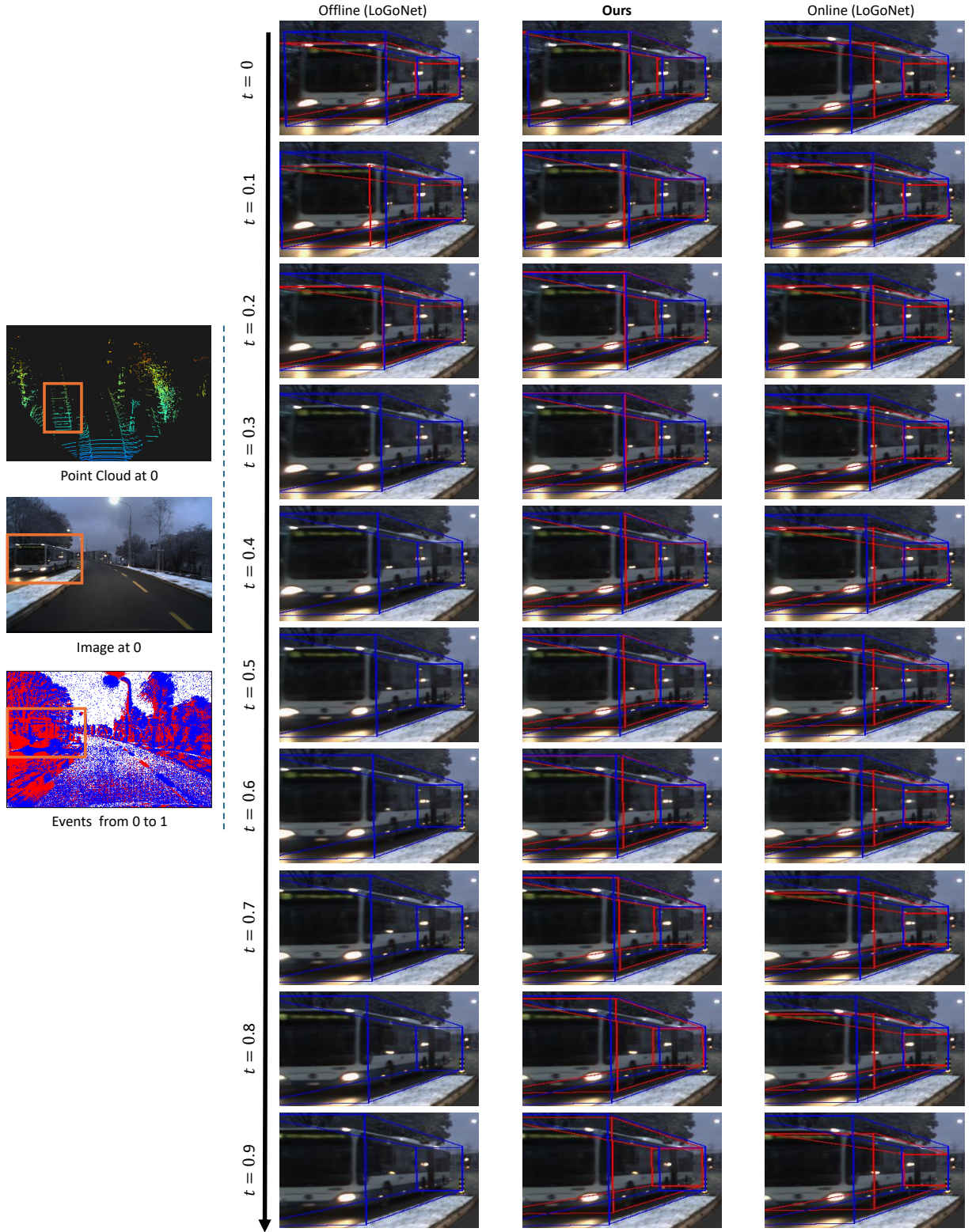


Figure 11. Qualitative comparisons with other offline and online methods on the DSEC-3DOD dataset. $t = 0$ represents the active time, while $t = 0.1, 0.2, 0.3, 0.4, 0.5, 0.6, 0.7, 0.8, 0.9$ denote the blind times. The **blue** box indicates ground truth, and the **red** box shows predictions. For better understanding, we overlaid the results onto the images generated by the interpolation method [37].

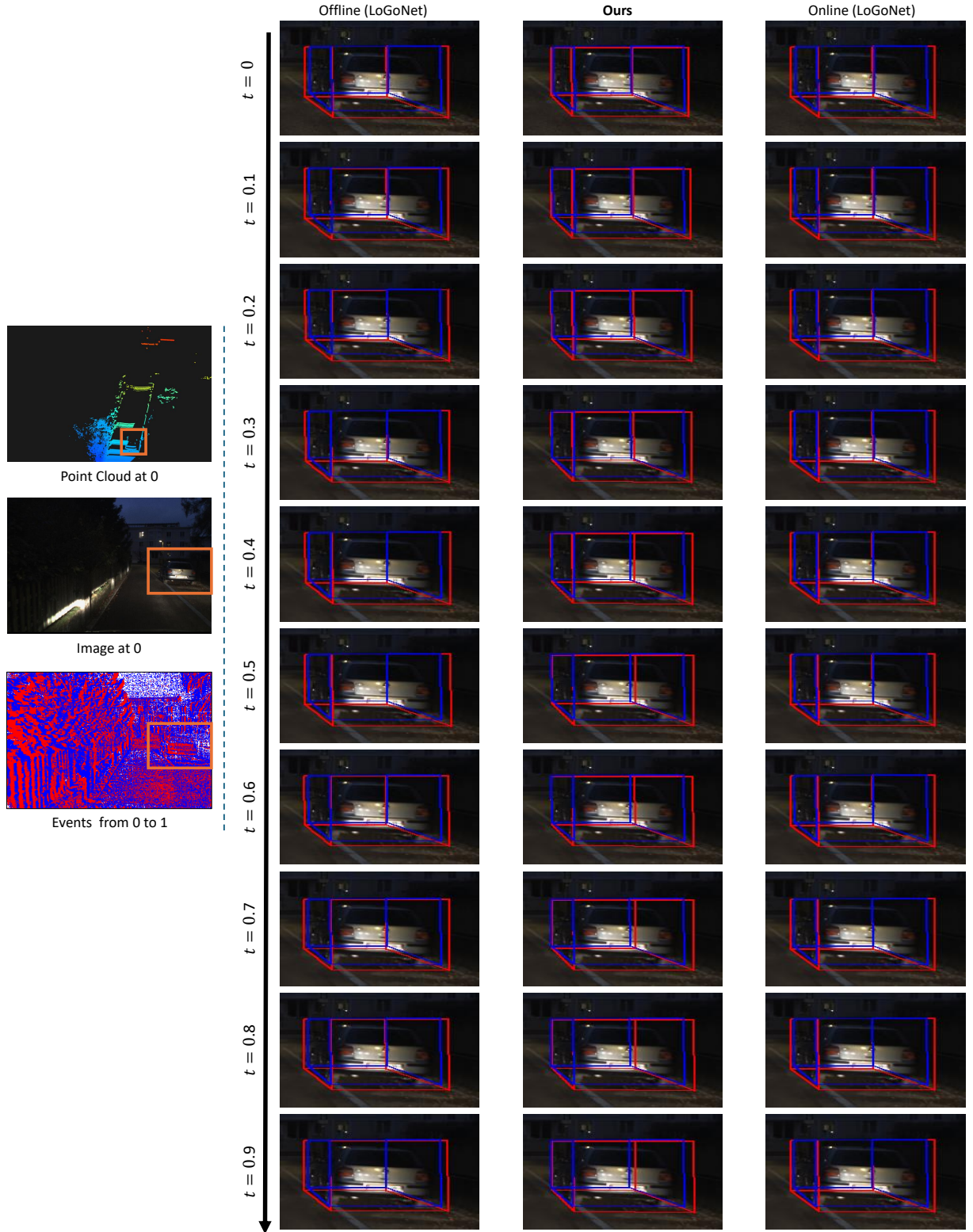


Figure 12. Qualitative comparisons with other offline and online methods on the DSEC-3DOD dataset. $t = 0$ represents the active time, while $t = 0.1, 0.2, 0.3, 0.4, 0.5, 0.6, 0.7, 0.8, 0.9$ denote the blind times. The blue box indicates ground truth, and the red box shows predictions. For better understanding, we overlaid the results onto the images generated by the interpolation method [37].

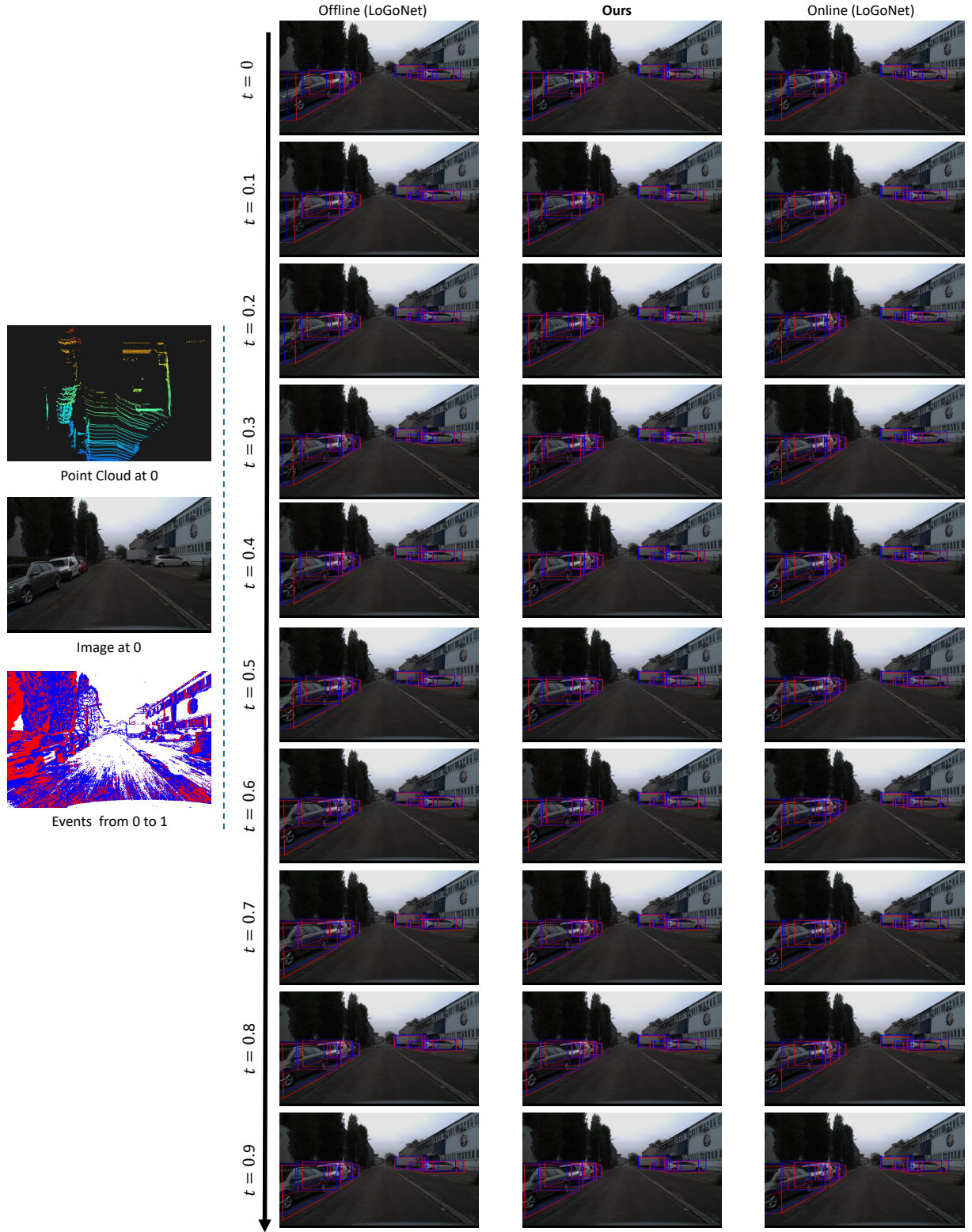


Figure 13. Qualitative comparisons with other offline and online methods on the DSEC-3DOD dataset. $t = 0$ represents the active time, while $t = 0.1, 0.2, 0.3, 0.4, 0.5, 0.6, 0.7, 0.8, 0.9$ denote the blind times. The blue box indicates ground truth, and the red box shows predictions. For better understanding, we overlaid the results onto the images generated by the interpolation method [37].

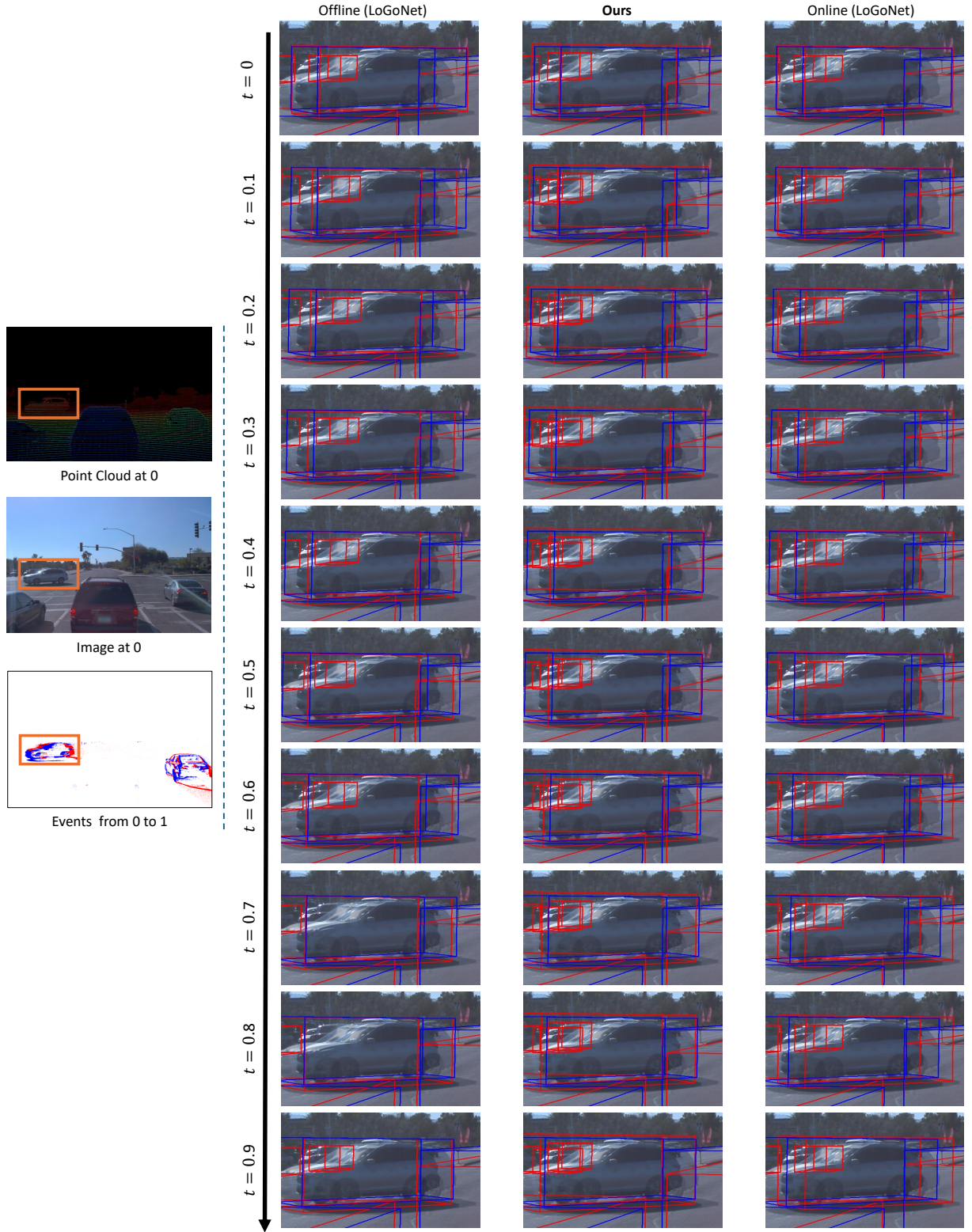


Figure 14. Qualitative comparisons of our method with other offline and online evaluations on the Ev-Waymo dataset. $t = 0$ represents the active time, while $t = 0.1, 0.2, 0.3, 0.4, 0.5, 0.6, 0.7, 0.8, 0.9$ denote the blind times. The blue box represents the ground truth, while the red box shows the prediction results of each method. For easier understanding, images at active timestamps 0 and 1 are overlaid.

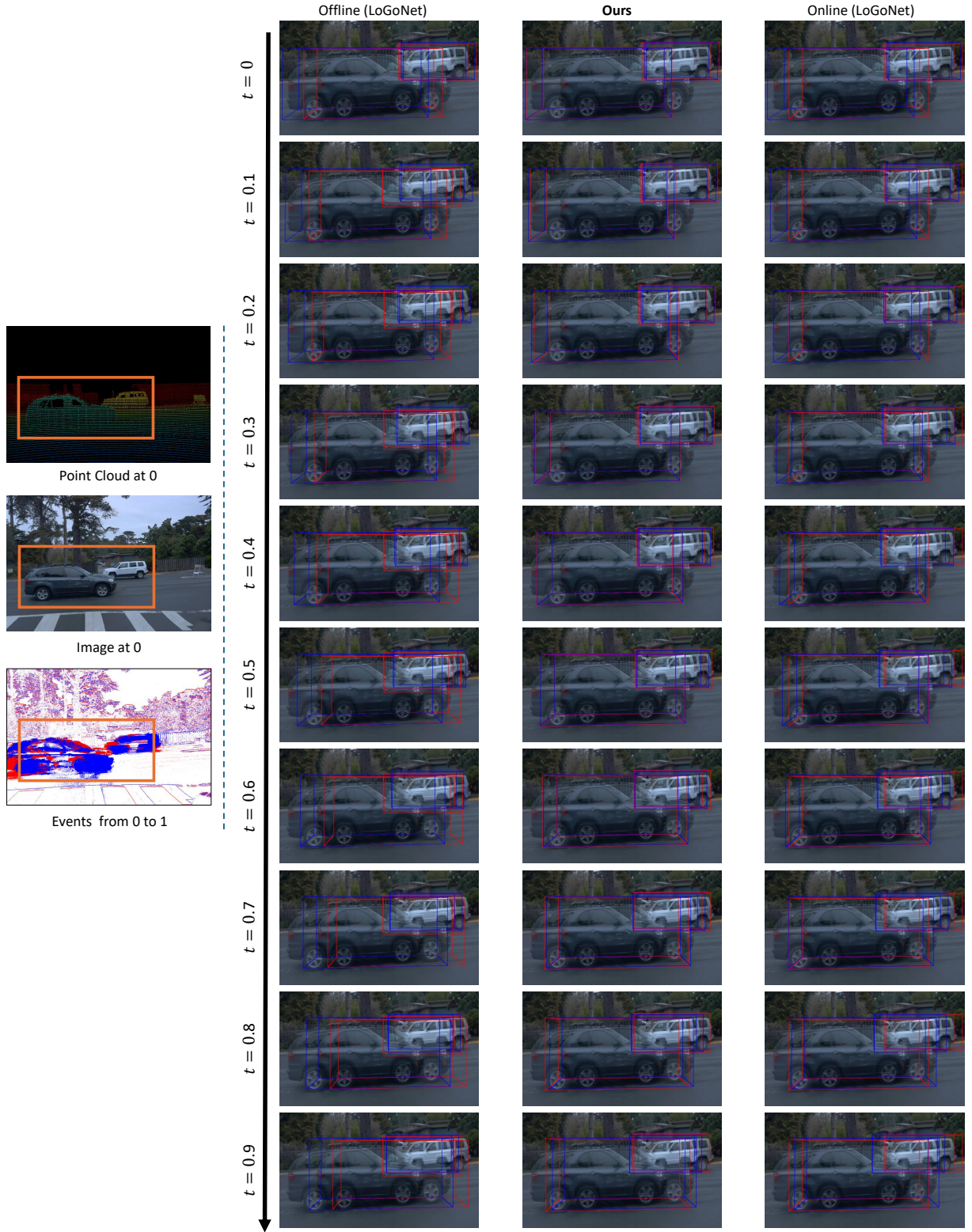


Figure 15. Qualitative comparisons of our method with other offline and online evaluations on the Ev-Waymo dataset. $t = 0$ represents the active time, while $t = 0.1, 0.2, 0.3, 0.4, 0.5, 0.6, 0.7, 0.8, 0.9$ denote the blind times. The blue box represents the ground truth, while the red box shows the prediction results of each method. For easier understanding, images at active timestamps 0 and 1 are overlaid.

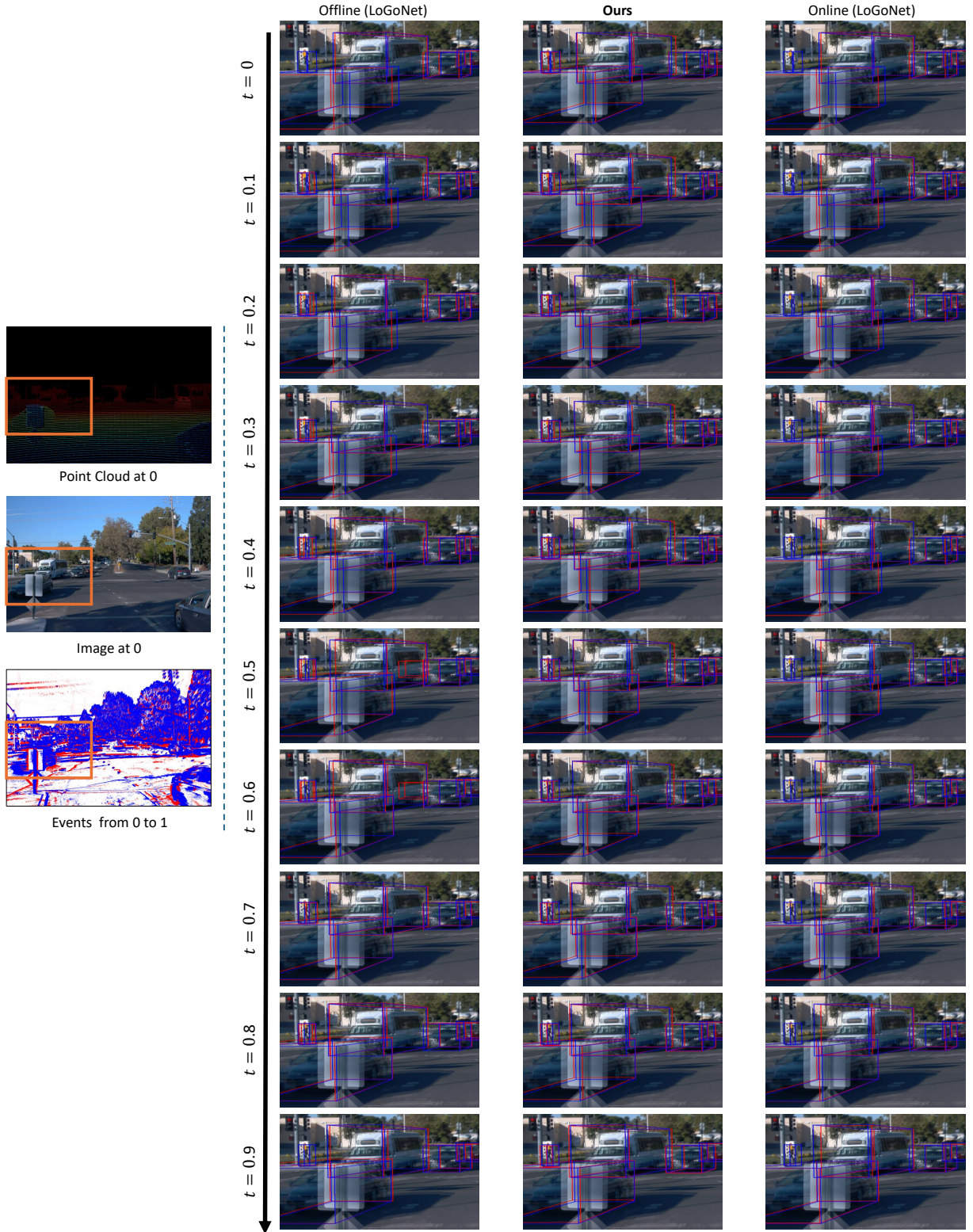


Figure 16. Qualitative comparisons of our method with other offline and online evaluations on the Ev-Waymo dataset. $t = 0$ represents the active time, while $t = 0.1, 0.2, 0.3, 0.4, 0.5, 0.6, 0.7, 0.8, 0.9$ denote the blind times. The blue box represents the ground truth, while the red box shows the prediction results of each method. For easier understanding, images at active timestamps 0 and 1 are overlaid.

Table 9. The train sequence splits of DSEC-3DOD dataset.

Split	Time	Sequence	# Frames	# GT Scenes
Train	Day	zurich_city_00_a	31	301
		zurich_city_00_b	155	1,505
		zurich_city_01_a	62	602
		zurich_city_01_b	155	1,505
		zurich_city_01_c	124	1,204
		zurich_city_01_d	93	903
		zurich_city_01_e	217	2,107
		zurich_city_01_f	155	1,505
		zurich_city_02_a	31	301
		zurich_city_02_b	124	1,204
		zurich_city_02_c	279	2,709
		zurich_city_02_d	155	1,505
		zurich_city_02_e	186	1,806
		zurich_city_04_a	93	903
		zurich_city_04_c	93	903
		zurich_city_04_d	93	903
		zurich_city_04_e	31	301
		zurich_city_04_f	124	1,204
		zurich_city_05_a	217	2,107
		zurich_city_05_b	124	1,204
		zurich_city_06_a	186	1,806
		zurich_city_07_a	124	1,204
		zurich_city_08_a	62	602
		zurich_city_11_a	31	301
		zurich_city_11_b	93	903
		zurich_city_11_c	155	1,505
	Day Total		3,193	31,003
	Night	zurich_city_03_a	62	602
		zurich_city_09_a	217	2,107
		zurich_city_09_b	31	301
		zurich_city_09_c	155	1,505
		zurich_city_09_d	124	1,204
		zurich_city_09_e	93	903
		zurich_city_10_a	248	2,408
		zurich_city_10_b	217	2,107
	Night Total		1,147	11,137
	Train Total		4,340	42,140

Table 10. The test sequence splits of DSEC-3DOD dataset.

Split	Time	Sequence	# Frames	# GT Scenes
Test	Day	zurich_city_00_a	62	602
		zurich_city_00_b	31	301
		zurich_city_01_e	31	301
		zurich_city_01_f	62	602
		zurich_city_02_b	31	301
		zurich_city_02_c	93	903
		zurich_city_02_d	62	602
		zurich_city_04_c	31	301
		zurich_city_04_d	31	301
		zurich_city_05_b	62	602
		zurich_city_06_a	31	301
		zurich_city_07_a	62	602
		zurich_city_08_a	31	301
		zurich_city_11_b	155	1,505
		zurich_city_11_c	93	903
	Day Total		868	8,428
	Night	zurich_city_03_a	31	301
		zurich_city_09_a	31	301
		zurich_city_09_c	31	301
		zurich_city_09_d	93	903
		zurich_city_10_a	31	301
		zurich_city_10_b	93	903
	Night Total		310	3,010
	Test Total		1178	11,438